Studies of Aluminum-Doped LiNi$_{0.5}$Co$_{0.2}$Mn$_{0.3}$O$_2$: Electrochemical Behavior, Aging, Structural Transformations, and Thermal Characteristics

Doron Aurbach,[a,*] Onit Srur-Lavi,[a] Chandan Ghanty,[a] Mudit Dixit,[a] Ortal Haik,[a] Michael Talianker,[b] Yehudit Grinblat,[a] Nicole Leifer,[a] Ronit Lavi,[a] Dan Thomas Major,[a,z] Gil Goobes,[a,z] Ella Zinigrad,[a] Evan M. Erickson,[a] Monica Kosa,[a] Boris Markovsky,[a,**,z] Jordan Lampert,[c] Aleksei Volkov,[c] Ji-Yong Shin,[c] and Arnd Garsuch[c]

[a]Department of Chemistry and the Lise Meitner-Minerva Center of Computational Quantum Chemistry, Bar-Ilan University, Ramat-Gan 52900, Israel
[b]Department of Materials Engineering, Ben-Gurion University of the Negev, Beer-Sheva 84105, Israel
[c]BASF SE, GCN/E, Ludwigshafen am Rhein 67056, Germany

This paper is dedicated to studies of the electrochemical behavior, the structural and thermal features of the Ni-rich LiNi$_{0.5}$Co$_{0.2}$Mn$_{0.3}$O$_2$ undoped and Al-doped ($\sim$0.01 at.%) materials for positive electrodes of lithium batteries. We have found that structural characteristics of these materials are quite similar from the crystallographic point of view. It was demonstrated that Al substitution in the doped LiNi$_{0.5}$Co$_{0.2}$Mn$_{0.3}$O$_2$ is preferred at Ni sites over Co sites, and the thermodynamic preference for Al^{3+} substitutions follows the order: Ni>Co>Mn. The lower capacity fading of the Al-doped electrodes upon cycling and aging of the cells in a charged state (4.3 V) at 60°C, as well as more stable mean voltage behavior, are likely due to the chemical and structural modifications of the electrode/solution interface. The Al-doped LiNi$_{0.5}$Co$_{0.2}$Mn$_{0.3}$O$_2$ electrodes demonstrate also lower resistances of the surface film and charge-transfer as well as lower activation energies for the discharge process. From XPS studies we conclude that the modified stable and less resistive interface on the Al-doped particles comprises the Li$^+$-ion conducting nano-sized centers like LiAlO$_2$, AlF$_3$, etc., which promote, to some extent, the Li$^+$ ionic transport to the bulk. A partial layered-to-spinel transformation was established upon cycling of LiNi$_{0.5}$Co$_{0.2}$Mn$_{0.3}$O$_2$ cathodes.
© 2015 The Electrochemical Society. [DOI: 10.1149/2.0681506jes] All rights reserved.

One of the major challenges in lithium batteries technology is, undoubtedly, the further improvement of battery components – electrodes, solutions, and separators.[1–7] Among several modern strategies to improve electrochemical performance and structural characteristics of materials for positive electrodes, doping has attracted the attention of scientists over the years. This is due to the effectiveness of dopants in stabilizing the structure of materials (even in minute amounts) and thus to increase the electrochemical cycling activity and to diminish the heat evolution of the electrodes in a charged state. A variety of dopant ions, like Co^{2+}, Al^{3+}, Ti^{4+}, Zr^{4+}, Zn^{2+}, Fe^{3+}, Cu^{2+}, and Cr^{3+}, has been used to improve the stability, morphology and microstructure of cathode materials, to enhance the electrode cycleability and rate capability, and to reduce capacity fading upon cycling.[8–13] For instance, doping of LiNi$_{0.5}$Mn$_{0.5}$O$_2$ with Co, Al, Ti resulted in decrease of the irreversible capacity loss and in almost no capacity fading of the doped electrodes.[14,15] In a systematic study of the Al-doped Ni-rich electrodes (LiNi$_{0.8}$Co$_{0.15}$Al$_{0.05}$O$_2$), which are promising materials for use in batteries for electromotive applications, the authors have shown high cycling stability of these electrodes upon accelerated testing.[16] Several other doping metals, such as silver, magnesium, cobalt, gallium, lanthanum, bismuth,[17–19] as well as non-metallic ions (boron, fluorine),[20,21] were also explored in an attempt to increase the electrochemical cycling behavior of cathodes (both of layered and spinel structures) and to reduce their interactions with electrolyte solutions. Alongside the cationic or anionic doping of the compounds for positive electrodes, another promising approach is surface modification of the materials with thin inactive coatings of oxides, fluorides, salts, etc., which also received extensive attention in the field.[22–27] Coatings prevent direct contact of the cathode material and solution species, thus improving the cycle life of lithium cells.[28] It should be noted that the effect of surface modification using oxides interrelates with metal doping since oxides form a thin surface layer containing "doped", distributed metal ions, with the host material (i.e. using Al$_2$O$_3$, or ZrO$_2$).[29,30] Our previous paper was dedicated to a complex study of the role of thin aluminum fluoride coatings on the electrochemical performance of (Li,Mn)-rich layered-layered (structurally

integrated) materials xLi$_2$MnO$_3$·(1-x)Li[MnNiCo]O$_2$ (x = 0.4-0.5).[31] In the present work, we focused on a comparative study of the electrochemical, aging, and thermal behavior and of structural characteristics of the Ni-rich LiNi$_{0.5}$Co$_{0.2}$Mn$_{0.3}$O$_2$ undoped and Al-doped materials in Li-cells. An intrigue question of this study was: How a small amount of Al-doping (0.01 at.%) at the expense of all transition metals (Ni, Co, Mn) influences the cycling performance, stability and capacity fading of LiNi$_{0.5}$Co$_{0.2}$Mn$_{0.3}$O$_2$ electrodes? Another motivating factor in this research was to understand the preference of Al doping at Mn, Co or Ni sites, a question which may be addressed by theoretical calculations of the substitution energies. It was also important to study the surface chemistry occurring in the Al-doped material in LiPF$_6$/alkyl carbonate solutions and its structural characteristics due to the interactions between the dopant and other species, a question addressed herein by solid-state NMR. We aimed furthermore to develop a deep understanding of the possible layered-to-spinel structural transformations in LiNi$_{0.5}$Co$_{0.2}$Mn$_{0.3}$O$_2$ electrodes upon cycling. Surprisingly, it was found that the ratio Ni/Ni+Co+Mn in the spinel structures, which were partially formed upon cycling of LiNi$_{0.5}$Co$_{0.2}$Mn$_{0.3}$O$_2$ electrodes, differed markedly from that of the initial layered phase. The novelty of this research lies in determining the impact of a minor Al-doping level on the electrochemical characteristics of LiNi$_{0.5}$Co$_{0.2}$Mn$_{0.3}$O$_2$ electrodes and on the interfacial reactions among the Al^{3+} dopant ions, Li$^+$ and F$^-$, while accounting for the local Li$^+$ structure. A new finding is also that aluminum may prevent, to some extent, the Ni leaching out from the bulk/surface of the LiNi$_{0.5}$Co$_{0.2}$Mn$_{0.3}$O$_2$ Al-doped sample, as confirmed by ^{7}Li and ^{27}Al NMR studies.

Experimental

Synthesis and characterization of LiNi$_{0.5}$Co$_{0.2}$Mn$_{0.3}$O$_2$ materials.— The Ni-rich LiNi$_{0.5}$Co$_{0.2}$Mn$_{0.3}$O$_2$ undoped and Al-doped compounds for positive electrodes of high-energy density lithium batteries were synthesized by BASF as experimental materials for these studies. In Table I, we present some structural characteristics of these materials, undoped and Al-doped LiNi$_{0.5}$Co$_{0.2}$Mn$_{0.3}$O$_2$, which are quite identical from the crystallographic point of view. The only difference is the Al-doping that was performed at a minor content of $\sim$0.01 at.% in the cost of all the transition metal (TM) ions of Ni, Co, and Mn. Hence, the formulae of the doped material

*Electrochemical Society Fellow.
**Electrochemical Society Active Member.
^{z}E-mail: majort@biu.ac.il; ggoobes@hotmail.com; markovskyboris22@gmail.com

Table I. Binding energies (eV) related to XPS peaks and their assignments measured from undoped and Al-doped LiNi$_{0.5}$Co$_{0.2}$Mn$_{0.3}$O$_2$ pristine and aged materials. Aging was carried out in EC-EMC/LiPF$_6$ solutions at 30°C during 14 days (magnetic stirring, Argon atmosphere).

Element	LiNi$_{0.5}$Co$_{0.2}$Mn$_{0.3}$O$_2$ samples			
	Undoped pristine	Undoped aged	Al-doped pristine	Al-doped aged
Li1s		56.2 w; 50.0 w (LiF)	55.5 (Li$_2$O); 55.2 st (Li$_2$CO$_3$)	56.7 st (LiF)
F1s	Not detected	685.9 st (LiF); 689.9 st (F–C bonds)	Not detected	685.7 st (LiF); 687.8 st (AlF$_3$); 689.9 st (F–C bonds)
O1s	531.7 st (surface oxygen; Li$_2$CO$_3$; LiOH)	533.1 st (O–C=O) 531.5 sh (O–C; Ni–OH)	531.7 st (surface oxygen; Li$_2$CO$_3$); 530–531 sh Al(OH)$_3$; Al$_2$O$_3$	531.5–532.3 st br (O–C; Ni–OH; Li$_2$CO$_3$); 533.3–533.5 sh (AlF$_2$OH; P–O–F; O–C=O)
Al2p	Not detected	Not detected	73.0–74.5 br (Al$_2$O$_3$)	73.0–76.0 br (LiAlO$_2$; Al$_2$O$_3$; Al$_2$F$_2$O$_2$); 77.4 w (AlF$_3$)
Ni2p3/2	854–857 br (Ni^{2+} in NiO; Ni^{3+} in Ni$_2$O$_3$)	854.0 sh (NiO)	854–857 br (NiO; Ni$_2$O$_3$)	858.0 st (LiNi$_x$Al$_y$O$_z$) 857.4–858.2 st (NiF$_2$)
P2p	Not detected	136 w (P – F)	Not detected	134 st (AlPO$_4$; P–O–F bonds)
Mn2p3/2	642.8 st (Mn^{4+} in MnO$_2$)	642.8 st (MnO$_2$)	642.8 st (MnO$_2$)	642.8 st (MnO$_2$)
Co2p1/2	797.4 st (Co^{3+} in Co$_2$O$_3$)	Co2p3/2 781.2 w (Co$_2$O$_3$; Co^{4+} in Co$_3$O$_4$)	797.4 st (Co$_2$O$_3$)	798.0 st (Co(OH)$_2$; Co2p3/2 782–783 br (CoF$_2$; CoF$_3$)
Mn2p1/2	654 br (Mn$_2$O$_3$; MnO$_2$)	654 br (Mn$_2$O$_3$; MnO$_2$)	654 br (Mn$_2$O$_3$; MnO$_2$)	654 br (Mn$_2$O$_3$; MnO$_2$)

Legends: st – strong peak; w – weak peak; sh – shoulder; br – broad peak

can be represented as LiNi$_{0.5-0.01x}$Co$_{0.2-0.01y}$Mn$_{0.3-0.01z}$Al$_{0.01(x+y+z)}$O$_2$. It should be also noted that these materials are characterized by very similar values of the following parameters: "slab thickness ratio Li/TM" and "Li-to-TM ratio" of 1.18 and 1.05 (for undoped) and 1.17 and 1.05 (for Al-doped), respectively. The chemical analysis of the materials was carried out using the inductive coupled plasma technique (ICP-AES, spectrometer Ultima-2 from Jobin Yvon Horiba). Their specific surface area was ∼0.4 m^2/g, as measured by the Brunauer, Emmett, and Teller (BET) method using a Gemini 2375, Micromeritics (multipoint mode). The crystallite size measured from XRD patterns of undoped and Al-doped LiNi$_{0.5}$Co$_{0.2}$Mn$_{0.3}$O$_2$ were 209 and 176 nm, respectively.

Electrochemical and aging measurements.— Electrochemical tests were carried out in two- and three-electrode cells in a 2325 coin-type and pouch-type configurations with a Celgard, Inc. polypropylene separator. The working electrodes were composites of a mixture of LiNi$_{0.5}$Co$_{0.2}$Mn$_{0.3}$O$_2$ materials (undoped or Al-doped), carbon black (CB) and polyvinylidene difluoride (PVdF) binder (80:10:10 by weight) on aluminum foil (from Strem). We prepared also thin-film working electrodes comprising only active LiNi$_{0.5}$Co$_{0.2}$Mn$_{0.3}$O$_2$ materials embedded into Al-foil by wiping. These electrodes were free from CB and PVdF, their thickness was ∼0.5 μm, as measured by focused ion-beam technique. Lithium disks or plates and lithium chips served as counter and reference electrodes. Electrochemical cells were assembled in glove boxes filled with highly pure argon (VAC, Inc.). We used electrolyte solutions (high purity, Li battery grade) comprising ethyl-methyl carbonate (EMC) and ethylene carbonate (EC) (weight ratio of 7:3) and 1M LiPF$_6$ from BASF. Thin-film LiNi$_{0.5}$Co$_{0.2}$Mn$_{0.3}$O$_2$ electrodes in pouch-cell configuration were tested in EC – EMC/LiPF$_6$ solutions containing 2% of vinylene carbonate (VC). The content of hydrofluoric acid and water in solutions was not more than 30 ppm and 10 ppm, respectively. After assembling, the electrochemical cells were stored at room temperature for 12–24 h to ensure a complete impregnation of the electrodes and the separators with the electrolyte solution. The electrochemical measurements were performed using a battery test unit model 1470, coupled with a FRA model 1255 from Solartron, Inc. (driven by Corrware and ZPlot software from Scribner Associates, Inc.), and a multichannel battery tester from Maccor, Inc., model 2000. For testing, we used a constant current mode in the potential range of 2.7–4. 3 V, at various current densities (C-rates). The alternating voltage amplitude in impedance measurements was 3 mV

and the frequency ranged from 100 kHz to 5 mHz. All the potentials in this paper are given vs. Li/Li$^+$. The accuracy of the calculations of the electrodes' capacity was around 95%. The electrochemical measurements were performed at 30°, 45°, and 60°C, in thermostats. At least 3 electrochemical cells comprising undoped or Al-doped electrode materials were tested at each temperature. Aging tests were carried out in contact of the Al-doped and undoped materials with EC – EMC/LiPF$_6$ solutions in polyethylene vials under argon atmosphere at 25°C for 10 days. This time is equivalent to galvanostatic cycling of the electrochemical cells containing LiNi$_{0.5}$Co$_{0.2}$Mn$_{0.3}$O$_2$ electrodes at a C/5 rate for ∼20 cycles.

X-ray diffraction (XRD), transmission electron microscopy (TEM) and electron diffraction (ED) analyses.— X-ray powder diffraction (XRD) measurements were performed using an AXS D8 Advance diffractometer from Bruker, Inc. (Germany) in the 2θ range from 10° to 110°, with a step size of 0.02°, at 15 sec/step rate. The analysis of the XRD patterns was carried out using the PowderCell program and the Fullprof program as described elsewhere.[32,33] HR-TEM examinations of the LiNi$_{0.5}$Co$_{0.2}$Mn$_{0.3}$O$_2$ material was performed with a JEOL JEM-2100 (LaB$_6$) high resolution electron microscope, and convergent beam electron diffraction (CBED) technique (4–7 nm probe size) was employed for structural characterization of nanoparticles. Samples for the TEM studies were prepared by methodology described in Ref. 34.

Analysis by solid-state nuclear magnetic resonance (NMR).— ^{19}F and ^{7}Li nuclei were probed on a Bruker 200 MHz at 188.28 MHz and 77.77 MHz, respectively, at spinning rates of 18–24 kHz, using single pulse and variable-τ Hahnecho sequences, which have the following pulse format: (90)$_x$ – τ – (180)$_y$ – τ - collect). All samples were externally referenced to KF(aq) at −125.3 ppm (CFCl$_3$ at 0 ppm) and LiF at 0 ppm (LiOH at 0 ppm), respectively. Single pulse and various echo sequences were implemented, as well as ^{19}F{^{27}Al} and {^{27}Al}^{19}F cross-polarization experiments. ^{19}F NMR data was collected on the cycled Al-doped material, as well as on the separators extracted from the cycled cells comprising LiNi$_{0.5}$Co$_{0.2}$Mn$_{0.3}$O$_2$ undoped and Al-doped samples.

Analysis by Raman spectroscopy and X-ray photoelectron spectroscopy (XPS) measurements.— Micro-Raman spectroscopy measurements were performed at room temperature using a micro-Raman
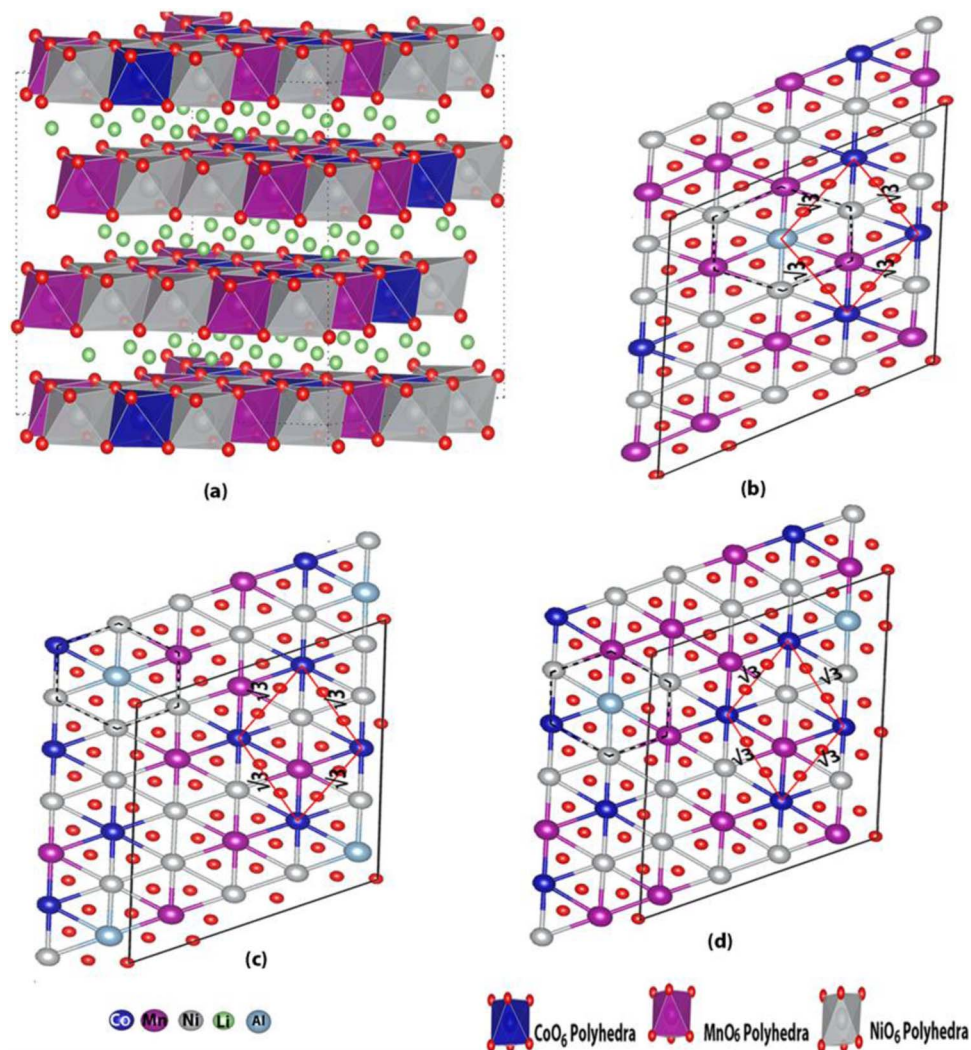
Figure 1. *(a)* Minimal energy structure of undoped $LiNi_{0.5}Co_{0.2}Mn_{0.3}O_2$. *(b)* Transition metal layer ordering in lowest energy structure of $Ni_{0.45}Co_{0.2}Mn_{0.3}Al_{0.05}O_2$, *(c)* $Ni_{0.5}Co_{0.2}Mn_{0.25}Al_{0.05}O_2$ and *(d)* $Ni_{0.5}Co_{0.15}Mn_{0.3}Al_{0.05}O_2$. Red lines indicate the $\sqrt{3}$ ordering parameter, strong black lines represent the supercell and dashed hexagon shows the surrounding of Al^{3+} ions in TM layer.

spectrometer from Renishaw inVia (United Kingdom) equipped with a 514 nm laser, a CCD camera, and an optical Leica microscope. Raman spectra were collected at least from 10–15 locations on a sample. The data were analyzed using Renishaw Wire 3.3 software. XPS measurements were performed in UHV (2.5×10^{-10} Torr base pressure) using 5600 Multi-Technique System (PHI, USA). The samples were irradiated with an Al K_{α} monochromated source (1486.6 eV) and the outcoming electrons were analyzed by a Spherical Capacitor Analyzer using the slit aperture of 0.8 mm. The charging of the samples during measurements has been compensated by the charge Neutralizer (C1s peak at 285 eV is used as the energy reference).

Computational methods.— All the calculations were performed using Density Functional Theory (DFT) as implemented in the Vienna ab inito simulation package (VASP)[35,36] with the plane wave pseudopotential based approach. We employed spin-polarized DFT within the generalized gradient approximation (GGA). Specifically, we used the Perdew, Burke and Ernzerhof (PBE) functional.[37] To represent the core electrons the projector augmented-wave (PAW)[38] method was used, and a kinetic energy cutoff of 400 eV was adopted. The system supercell used in all the calculations consisted of 5×4 unit cells, with 60 formula units of $R\bar{3}m$ (α-NaFeO$_2$ type) layered structure. Due to the large supercell, the Brillouin zone was sampled with the gamma point only. Although antiferromagnetic calculations

give useful insights about the electronic structure, in the current case these do not change the energy differences between the structures significantly.[39] Since the magnetic structure of $LiNi_{0.5}Co_{0.2}Mn_{0.3}O_2$ is unknown, we have thus assumed ferromagnetic spin ordering.

Results and Discussion

Computational studies of the preferred configurations for the Al-doping in $LiNi_{0.5}Co_{0.2}Mn_{0.3}O_2$ material.— Previous theoretical studies show that transition metals in layered lithiated oxide materials exhibit different in-plane ordering depending on their formal oxidation state.[40–43] In a recent study,[44] Yu et al. have defined the ordering parameters to describe the cationic ordering. Following similar approach, we considered cationic orderings for TMs with different ordering parameters. The structures with $\sqrt{3}$ ordering parameter (Figure 1b) for cobalt and manganese are comparatively more stable than that structure with alternative ordering parameters. This is in agreement with previous experimental and theoretical reports on similar classes of materials.[41,44] Figure 1a shows the lowest energy supercell for undoped $LiNi_{0.5}Co_{0.2}Mn_{0.3}O_2$ with $\sqrt{3}$ ordering parameter for Co.

Configurational energy calculations.— To understand the structural changes on TM substitution with Al, one TM ion is substituted with one Al ion in each layer (a total of three Al atoms in the
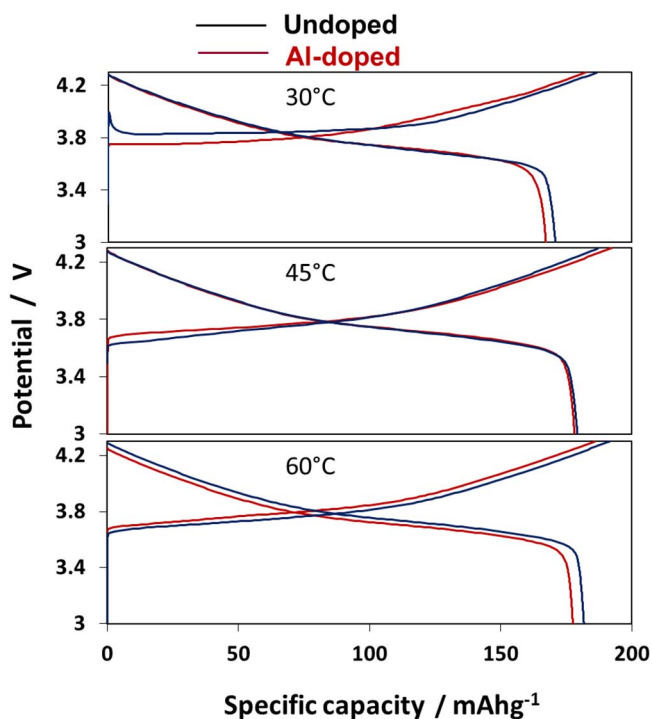
Figure 2. Voltage profiles of $LiNi_{0.5}Co_{0.2}Mn_{0.3}O_2$ electrodes at various temperatures (as indicated) measured from the first cycles at a C/15 rate.

supercell) i.e. resulting in the formula $LiNi_{0.5}Co_{0.15}Mn_{0.3}Al_{0.05}O_2$ (in case of Co substituted). Practically, the in-silico Al concentration (0.05) was greater than the experimental concentration (0.01), due to computational considerations. We considered 3, 4 and 6 Al doped configurations for Co, Mn and Ni ions, respectively. Our results suggest that by substituting the Mn-ions with Al^{3+}, in the most preferred configuration (relative energy 0.17 eV), Al^{+3} is surrounded by 4 Ni, 1 Mn, and 1 Co-ions (Figure 1c), which possesses the lowest energy when compared with other Mn substituted configurations. In the most preferred Co ions substituted configuration (relative energy 0.14 eV, Figure 1b), Al^{3+} is in $(\sqrt{3} \times \sqrt{3})$ R30°[45,46] type of motif. In the lowest energy Ni ion substituted configuration (relative energy −0.74 eV), Al^{+3} is surrounded by 1 Co, 2 Mn and 3 Ni ions (Figure 1d).

Substitution energy calculations.— To demonstrate the preference of Al substitution on Mn, Co and Ni sites, we calculate the substitution energy per Al ion, defined here as:

$$E_{subs} = \frac{1}{3}\{(E_{Al-NCM} + 3E_{TM}) - (E_{NCM} + 3E_{Al})\} \qquad [1]$$

where E_{Al-NCM} is the total energy of Al doped Ni-Co-Mn (NCM) $LiNi_{0.5}Co_{0.2}Mn_{0.3}O_2$ material, E_{NCM} is the total energy of the undoped material. E_{TM} and E_{Al} are the energies of transition metals and aluminum in ground state metallic structure. The substitution energies of the configurations doped at the preferred Co, Mn and Ni sites are −5.13 eV, −3.10 eV and −5.86 eV, respectively. Clearly, the highest negative substitution energy of Al substitution at Ni sites confirms that Al substitution is preferred at Ni sites over Co sites. The thermodynamic preference of Al^{+3} substitutions follows the order: Ni>Co>Mn. The local magnetic moments of undoped $LiNi_{0.5}Co_{0.2}Mn_{0.3}O_2$ suggest that the formal charges on Co and Mn are +3 and +4, respectively. Interestingly, our calculations suggest that there is an existence of both Ni^{+2} (magnetic moment ~1.5) and Ni^{+3} ions (magnetic moment ~0.8) in both doped and undoped pristine material. A detailed study of the above issues including different magnetic ordering with various cationic orderings of undoped and Al-doped $LiNi_{0.5}Co_{0.2}Mn_{0.3}O_2$ materials will appear in a separate paper from our groups.

Electrochemical and aging behavior of $LiNi_{0.5}Co_{0.2}Mn_{0.3}O_2$ electrodes.— In Figure 2, we present typical voltage profiles of the first charge/discharge cycles measured from undoped and Al-doped $LiNi_{0.5}Co_{0.2}Mn_{0.3}O_2$ electrodes at 30, 45, and 60°C in the potential range of 3.0–4.3 V at a C/15 rate. In general, upon charge from OCV to the cutoff potential of 4.3 V, the capacity monotonously increases, in correlation with the literature data.[47] We observed at 30°C that the electrode potential for the undoped material suddenly increases to ~4 V in the first charge, decreases to ~3.8 V, and then increases slowly. This voltage change is well known phenomenon,[47] however, its origin is still unclear. It may relate to some energy barriers for the initial formation of a partially delithiated phase in $LiNi_{0.5}Co_{0.2}Mn_{0.3}O_2$ during the first Li^+ extraction. It was established that undoped and Al-doped $LiNi_{0.5}Co_{0.2}Mn_{0.3}O_2$ electrodes exhibit similar irreversible capacity losses (ICL) at 30, 45, and 60°C calculated as average values from 3 parallel tests at each temperature. At the same time, ICL of both types of electrodes slightly decreases from ~8.3 to ~5.1 mAh/g with increasing the temperature. This can be partially related to lesser effects of side reactions on the well passivated electrode surface at higher temperature due to the optimized chemical and structural properties of the solid-electrolyte interface (SEI). We have found that the electrochemical behavior of electrodes comprising undoped and Al-doped $LiNi_{0.5}Co_{0.2}Mn_{0.3}O_2$ materials is stable upon cycling at 30, 45, and 60°C. Figure 3a, 3b demonstrates typical plots of the electrode capacity and Coulombic efficiency vs. cycle number at 30°C (similar results
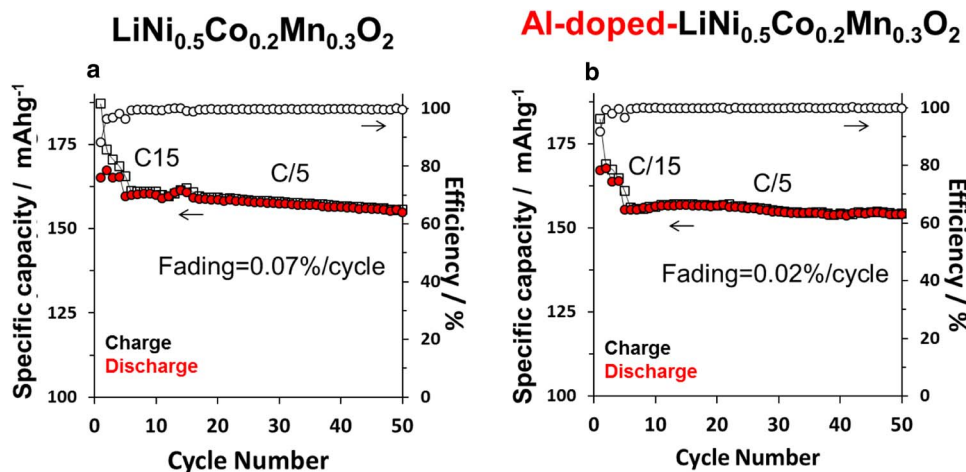

Figure 3. Cycling performance of $LiNi_{0.5}Co_{0.2}Mn_{0.3}O_2$ electrodes at 30°C in coin-type cells. Potential range was 3.0–4.3 V.

obtained at 45 and 60°C are not shown). The results of the discharge capacity fade show that although undoped $LiNi_{0.5}Co_{0.2}Mn_{0.3}O_2$ electrodes exhibit slightly higher reversible capacity, its fade is ∼3 times greater in comparison with Al-doped electrodes at 30°C. At higher temperatures, this improvement of the Al-doped electrode material becomes less noticeable and capacity fade increases for both types of electrodes to ∼0.12 – 0.2% per cycle at 60°C possibly due to their surface and structural changes at elevated temperatures. For reliability reasons, the average capacity fading values were calculated from 3 parallel tests at each temperature; additionally, only the first 25 cycles at a C/5 rate were purposely selected to calculate the capacity loss. The reason is that upon short cycling duration at moderate currents, the Li dissolution/deposition processes at the negative electrodes (Li-metal) in alkyl carbonates solutions can be considered as quasi-reversible and uniform ensure therefore the Li balance in the cell. In contrast, prolonged cycling and high rates result in extremely non-uniform lithium deposition, severe morphological changes, breaking down the surface films and even the lithium dendrites formation.[48] These may interfere badly to the cycling behavior of the positive electrodes and cause the capacity fading. We have established that upon short-term testing, the Al-doped $LiNi_{0.5}Co_{0.2}Mn_{0.3}O_2$ electrodes demonstrate lower activation energies E_a^* of the discharge process and therefore faster lithiation. The activation energy values of discharge vary from 1.14 to 0.54 kJ/mole for the Al-doped $LiNi_{0.5}Co_{0.2}Mn_{0.3}O_2$ electrodes and from 2.85 to 1.73 kJ/mole for their undoped counterparts during the first 25 cycles at a C/5 rate. The activation energies were calculated from the Arrhenius equation: $C_{disch} = A_0 e^{-E_a^*/RT}$, where C_{disch} stands for the discharge capacity, A_0 is a constant, R = 8.314 J/mole·K and T are the gas constant and the absolute temperature, respectively. The reliability factors for the linear regression lines of E_a^* vs. 1/T were in the range of R^2 = 0.973–0.988. The E_a^* values obtained are in a quantitative agreement with those demonstrated in the literature for the discharge processes of the Ni-rich Al-doped $LiNi_{0.8}Co_{0.15}Al_{0.05}O_2$ electrodes during prolonged cycling in full cells.[16] The lower activation energies for the Al-doped electrodes correlate with our observation of the lower differences between anodic and cathodic peaks potentials δ = E_{an} − E_{cath} measured from the slow potential scan rate CVs (ν = 10–50 μV/s) of the Al-doped $LiNi_{0.5}Co_{0.2}Mn_{0.3}O_2$ electrodes (δ = 10 mV comparing to δ = 30 mV for undoped ones) that point to faster kinetics of these electrodes. It is therefore assumed that doping enhances, to some extent, the electrochemical kinetics and reversibility of doped electrodes, in line with the literature reports.[49] Another evidence of faster kinetics is the lower potential difference (δ) for all the scan rates measured from thin-film electrodes comprising Al-doped material at 45°C (these electrodes were free of PVdF and carbon black). We suggested that the peak current densities of $LiNi_{0.5}Co_{0.2}Mn_{0.3}O_2$ electrodes follow the equation[50] that establishes the proportionality of the CV peak currents (I_p) to $ν^{1/2}$: $I_p = 2.69 \times 10^5 n^{\frac{3}{2}} A D_{Li}^{\frac{1}{2}} ν^{\frac{1}{2}} C_0$, where n is the number of electrons (n = 1 for the Li^+), A the electrode's geometric surface area, D_{Li} the chemical diffusion coefficient of Li^+ in the electrode, and C_0 represents the Li^+ concentration in the cathode bulk.

Indeed, the dependences of the anodic and cathodic peak currents on the potential scan rate demonstrate the slopes close to 0.5 both for undoped and Al-doped electrodes indicating diffusion controlled processes of Li^+ intercalation/deintercalation. In Figure 4, we compare typical slow scan rate cyclic voltammograms of undoped and Al-doped $LiNi_{0.5}Co_{0.2}Mn_{0.3}O_2$ electrodes at 30°C. These CVs demonstrate quite reversible electrochemical behavior with well resolved anodic/cathodic peaks related to the Li-extraction/insertion accompanied with the Ni^{2+}/Ni^{4+} and Co^{3+}/Co^{4+} oxidation/reduction, respectively. Although undoped electrodes exhibit more pronounced splitting into two oxidation peaks around 3.7–3.8 V, the Al-doping results in lower separation $δ_{1,2} = E_{an1} − E_{an2}$ between these peaks, namely 40 mV in comparison with ∼70 mV for undoped electrodes. Similar results were obtained from cyclic voltammograms (ν = 10 μV/s, 45°C) of thin-film electrodes comprising only active materials (no PVdF and carbon black).
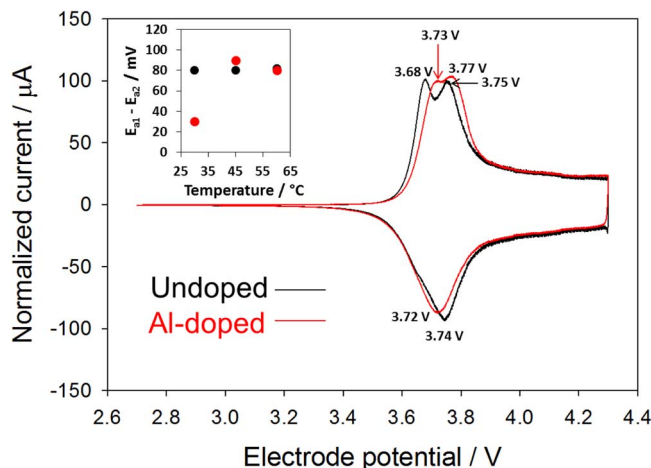

Figure 4. Slow scan rate (10 μV/s) CVs of $LiNi_{0.5}Co_{0.2}Mn_{0.3}O_2$ electrodes measured at 30°C in coin-type cells. *Insert*: Evolution of the anodic peaks separation $E_{a1} − E_{a2}$ with temperature of undoped (black circles) and Al-doped (red circles) $LiNi_{0.5}Co_{0.2}Mn_{0.3}O_2$ electrodes measured from the differential capacity plots in Figure 5.

Comparing of differential capacity plots obtained from composite $LiNi_{0.5}Co_{0.2}Mn_{0.3}O_2$ electrodes at various temperatures also demonstrate at 30°C lesser anodic peaks separation $δ_{1,2}$ in charge for the Al-doped material (Figure 5). This is indicative of more favorable charge processes of these electrodes in comparison with the undoped ones that correlates with the lower mean voltage values in charge of the Al-doped $LiNi_{0.5}Co_{0.2}Mn_{0.3}O_2$. However, at 45 and 60°C both electrodes show similar anodic peaks separation that may point to comparable kinetics of the Li^+ extraction and transition metals oxidation upon charge.

An interesting piece of information to compare undoped and Al-doped materials was extracted from combined cycling/aging experiments. First, the cells comprising undoped and Al-doped $LiNi_{0.5}Co_{0.2}Mn_{0.3}O_2$ electrodes were cycled at a C/5 rate (30°C), terminated at 4.3 V (charged state, Li^+ is partially extracted) and then were exposed to aging at 60°C for 7 days followed by further cycling at 30°C. The results of these cycling/aging experiments demonstrate that the potential decay dE/dt during the first 24 h of aging is comparable for undoped and Al-doped materials (1.29 and 1.27 mV/h, respectively), while the capacity fade during aging in a charged state is less for the Al-doped electrodes (0.051 mAh/g vs. 0.072 mAh/g). Another important improvement of the Al-doped electrodes is that their capacity fade after aging at 60°C is much lower in comparison with their undoped counterparts (0.34 and 2.59%, respectively). One more significant parameter extracted from the results of cycling and aging experiments of the above electrodes is mean voltage in charge and discharge as a function of cycle number. These results demonstrate that *(i)* the evolution of mean voltage in charge upon continuous cycling and during aging is similar for the undoped and Al-doped materials, and *(ii)* aging in a charged state (4.3 V, 60°C) stabilizes mean voltage in charge and discharge. It was shown also that mean voltage in discharge increases by ∼40 mV and in charge it decreases by ∼20 mV for Al-doped electrodes indicating thus a lower total polarization of these electrodes comparing to the undoped ones. This is likely due to the chemical and structural modifications of the electrode/solution interface upon cycling and storage the electrodes in a charged state at 60°C. In the following sections, we discuss possible interfacial reactions of Al-doped electrodes that result in formation of Li-[Al-O], Li-[Al-F], and other species. Attention is also paid to lower resistances measured from impedance spectra of Al-doped electrodes upon cycling and aging in a charged state.

Impedance studies of $LiNi_{0.5}Co_{0.2}Mn_{0.3}O_2$ electrodes.— Our assumption on more stable and, to some extent, less resistive

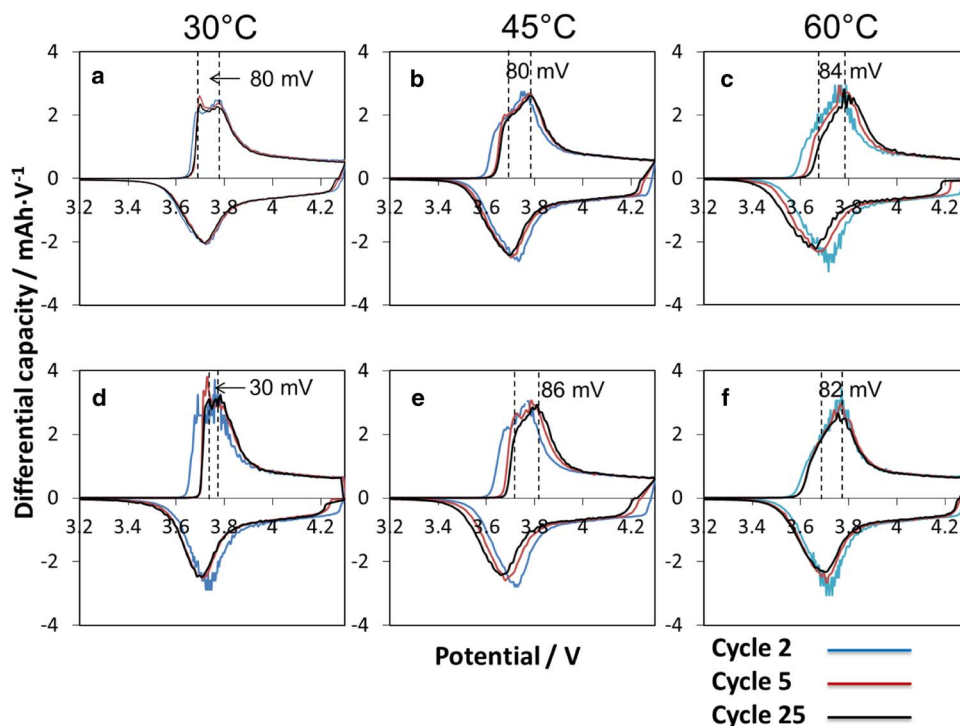**Figure 5.** Differential capacity of LiNi$_{0.5}$Co$_{0.2}$Mn$_{0.3}$O$_2$ undoped *(a, b, c)* and Al-doped *(d, e, f)* electrodes measured at various temperatures. The anodic peaks separations E$_{an1}$ − E$_{an2}$ (mV) calculated from 25-th cycle at each temperature are indicated. Blue curves – 2-nd cycle, red – 5-th cycle, black – 25-th cycle.

electrode/solution interface of the Al-doped LiNi$_{0.5}$Co$_{0.2}$Mn$_{0.3}$O$_2$ electrodes has been verified by the impedance measurements upon charge at 3.9 and 4.3 V. For this purpose, we explored thin-film electrodes comprising only LiNi$_{0.5}$Co$_{0.2}$Mn$_{0.3}$O$_2$ active material without any additives (PVdF and carbon black). These electrodes were cycled at 45°C at various C-rates as demonstrated in Figure 6, which compares the normalized discharge capacities of LiNi$_{0.5}$Co$_{0.2}$Mn$_{0.3}$O$_2$ undoped and Al-doped electrodes. They show comparable capacities at moderate rates, while the doped material delivers slightly superior capacities at higher currents. Moreover, the capacity fade of these electrodes after cycling and aging in a charged state (4.3 V) is slightly lower in comparison with their undoped counterparts. The above electrochemical parameters correlate with lower impedances of the Al-doped electrodes measured at 3.9 and 4.3 V after cycling/aging (Figure 7). It was established that the Al-doped thin-film electrodes indeed demonstrate lower resistances of the Li$^+$ migration through the surface film R$_{sf}$ (a small semicircle at high frequencies from 200 kHz to 5 kHz in Z$'$, −Z$''$-plots) and of the charge-transfer R$_{ct}$ (a depressed semicircle in the intermediate frequency domain, 50 Hz–1 Hz) measured at 3.9 V and 4.3 V during the charge process. Typically, at these potentials the surface-film resistance R$_{sf}$ of the Al-doped LiNi$_{0.5}$Co$_{0.2}$Mn$_{0.3}$O$_2$ electrodes cycled and subsequently aged in a charged state is almost twice lower in comparison with that of the undoped ones. The evolution of the charge-transfer resistance R$_{ct}$ with the electrode potential and cycling/aging of undoped and Al-doped electrodes is shown in Figure 8 that demonstrates lower R$_{ct}$ of the latter electrodes upon charge to 4.3 V. These results are in agreement with those obtained by other groups.[51,52] As it follows from the literature data, the Al-doping leads to lower impedance of doped LiCoO$_2$ electrodes in comparison with that of the undoped material.[51] Moreover the charge-transfer resistance was shown to be reduced by the Al or Co-doping of LiNi$_{0.5}$Mn$_{0.5}$O$_2$ electrodes.[52,53] In Figure 7, the inclined lines in the low frequency domain (up to 5 mHz) of the impedance spectra reflect the solid-state Li$^+$ diffusion in the bulk (Warburg impedance). Presumably, the Li$^+$ diffusion coefficient (D$_{Li}$) is comparable for the undoped and Al-doped materials due to their similar morphological and crystallographic characteristics and minor content of the dopant.

Almost equal slopes of the peak currents vs. scan rate plots, both in charge and in discharge furthermore point that lithium-ion diffusion coefficients of undoped and Al-doped LiNi$_{0.5}$Co$_{0.2}$Mn$_{0.3}$O$_2$ should be similar (the calculation of D$_{Li}$ for these materials was beyond the scope of this study). In a recent literature report, a similarity of D$_{Li}$ around 10^{-15} cm^2/s has also been established for undoped and Fe-doped Li$_{1.2}$Mn$_{0.6}$Ni$_{0.2}$O$_2$ electrode materials.[54] It is important to emphasize that the above impedance spectra (Figure 7) reflect the resistances produced *only* by the active cathode materials because the undesired reactions of PVdF and carbon black additives affecting the surface film formation and charge-transfer were avoided in these electrodes. We note also that the impedance performance of the
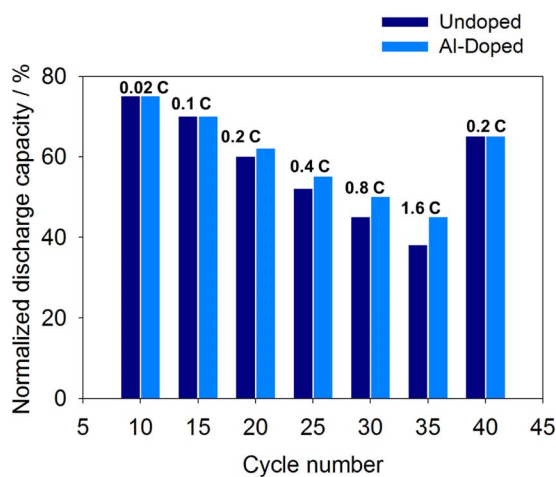

Figure 6. Normalized discharge capacities of thin-film electrodes (∼0.5 μ) comprising only active cathodes materials of undoped and Al-doped LiNi$_{0.5}$Co$_{0.2}$Mn$_{0.3}$O$_2$ as a function of cycle number. These electrodes were free of PVdF and carbon black. Cycling was performed at 45°C; rates of cycling are indicated.
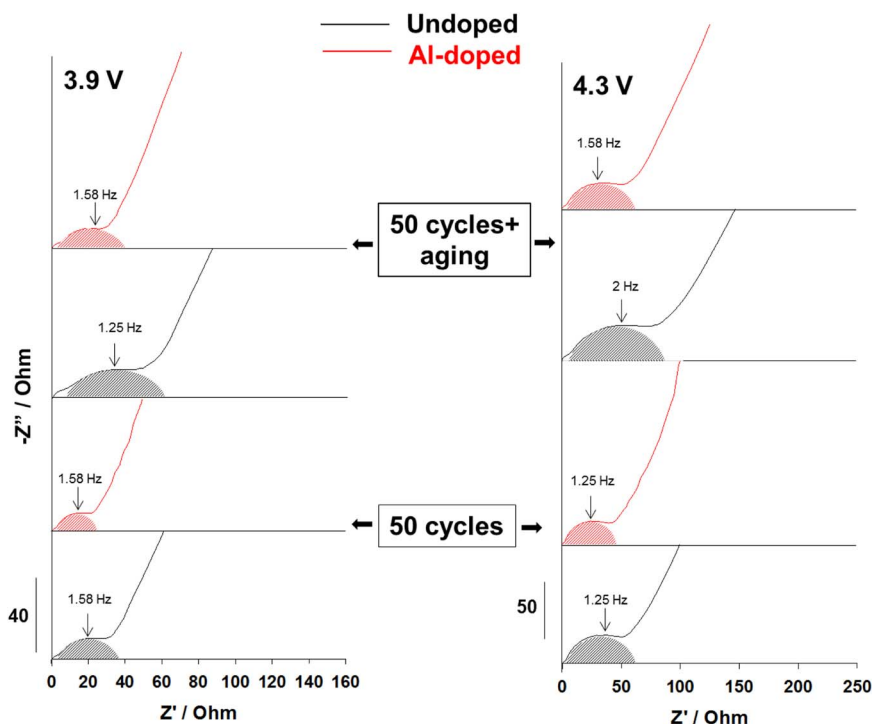
Figure 7. Impedance spectra of thin-film LiNi$_{0.5}$Co$_{0.2}$Mn$_{0.3}$O$_2$ electrodes ($\sim$0.5 µm) comprising only undoped (black curves) and Al-doped (red curves) materials measured at 3.9 V and 4.3 V at 45°C in pouch-cells. These electrodes were free of PVdF and carbon black additives. The cells underwent 40 cycles at various C-rates followed by a subsequent aging for 10 days in a charged state (4.3 V, 45°C). In these spectra, semicircles (registered at the intermediate frequencies) relate to the interfacial charge-transfer resistances of LiNi$_{0.5}$Co$_{0.2}$Mn$_{0.3}$O$_2$ electrodes. The semicircles are marked with black and red patterns, respectively for undoped and Al-doped electrodes.

Al-doped LiNi$_{0.5}$Co$_{0.2}$Mn$_{0.3}$O$_2$ electrodes resembles a similar behavior of the layered-layered structurally integrated materials coated with AlF$_3$, the presence of which, though at a low content, resulted in more stable electrochemical and aging behavior comparing to their uncoated counterparts, as studied in our recent work.[31]
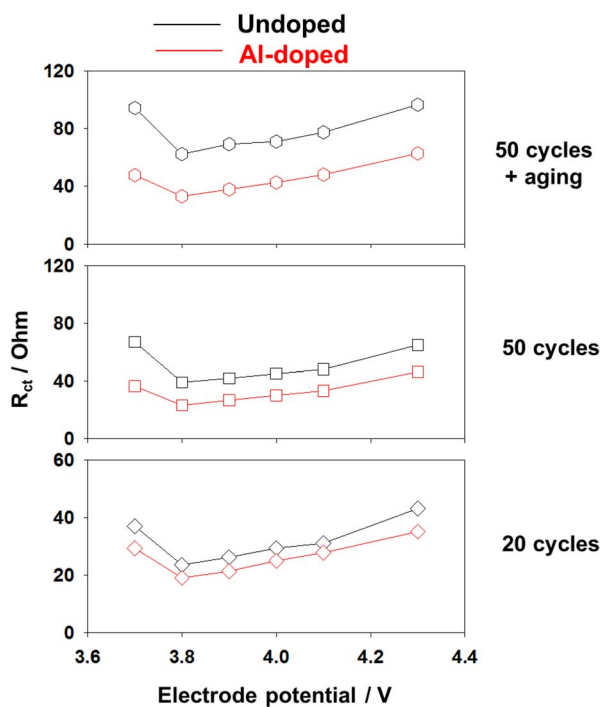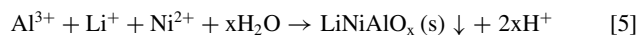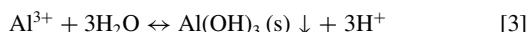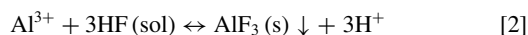

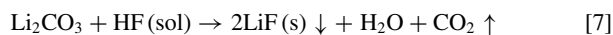**Figure 8.** Charge-transfer resistance R$_{ct}$ measured from impedance spectra of thin-film LiNi$_{0.5}$Co$_{0.2}$Mn$_{0.3}$O$_2$ electrodes comprising only undoped and Al-doped materials as a function of the electrode potential and cycling/aging. These electrodes were free of PVdF and carbon black additives. Aging after 40 cycles at various C-rates was carried out in a charged state of 4.3 V for 10 days at 45°C.

Interfacial LiNi$_{0.5}$Co$_{0.2}$Mn$_{0.3}$O$_2$/solution reactions and XPS analysis.— We suggest that improved, to some extent, electrochemical and aging performances of Al-doped electrodes may relate to more stable cathode/solution interface and, consequently, to lower the surface film and charge-transfer resistances resulted from specific surface interactions of these electrodes with solution species. A hypothesis is that upon cycling or aging in solutions, a thin reactive surface layer (RSL) on the particles of the Al-doped material becomes enriched with Al^{3+}-ions, which initiate the following interfacial reactions:

$$Al^{3+} + 3HF\,(sol) \leftrightarrow AlF_3\,(s) \downarrow + 3H^+ \qquad [2]$$

$$Al^{3+} + 3H_2O \leftrightarrow Al(OH)_3\,(s) \downarrow + 3H^+ \qquad [3]$$

$$Al^{3+} + Li^+ + 4HF \leftrightarrow Li[AlF]_4\,(s) \downarrow + 4H^+ \qquad [4]$$

$$Al^{3+} + Li^+ + Ni^{2+} + xH_2O \rightarrow LiNiAlO_x\,(s) \downarrow + 2xH^+ \qquad [5]$$

$$Al^{3+} + Li^+ + 4H_2O \rightarrow LiAlO_2\,(s) \downarrow + 4H^+ \qquad [6]$$

It is reasonable to propose that Al-containing species formed in a thin RSL upon cycling or aging in solutions of Al-doped electrodes may partially suppress an unavoidable formation of LiF (by reactions 7 and 8), stabilize the electrode/solution interface and, hence, lead to lower impedance and more stable charge-discharge behavior of these electrodes:

$$Li_2CO_3 + HF\,(sol) \rightarrow 2LiF\,(s) \downarrow + H_2O + CO_2 \uparrow \qquad [7]$$

$$Li_2CO_3 + PF_5 \rightarrow CO_2 \uparrow + 2LiF\,(s) \downarrow + POF_3 \uparrow \qquad [8]$$

It should be noted that phosphorous oxyfluoride POF$_3$ (reaction 8) can also react with water and HF in solution to form several fluorinated phosphoric acids (for instance, H$_2$PO$_3$F), which further interact with water and produce hydrofluoric and phosphoric acids:[55]

$$H_2PO_3F + H_2O \rightarrow HF + H_3PO_4 \qquad [9]$$
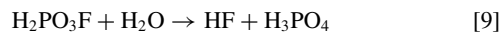
Hence, along with the reactions 1–5, the following reaction may take place at the electrode/solution interface producing the aluminum phosphate species:

$$Al^{3+} + 3PO_4{}^{3-} + H_2O \rightarrow AlPO_4 \cdot H_2O\,(s) \downarrow \qquad [10]$$

Table II. The results of Rietveld profile fitting of pristine undoped and Al-doped $LiNi_{0.5}Co_{0.2}Mn_{0.3}O_2$ materials and of the corresponding electrodes cycled at 30°C.

Material	Material's condition	a (Å)	c (Å)	Unit cell volume (Å^3)	R$_p$-factor of refinement (%)
$LiNi_{0.5}Co_{0.2}Mn_{0.3}O_2$	Pristine	2.8667	14.2136	101.2	2.42
	Charged 4.3 V after 5 cycles	2.8139	14.2591	97.8	4.25
	Discharged 3.0 V after 5 cycles	2.8631	14.1465	100.43	5.63
$LiNi_{0.5}Co_{0.2}Mn_{0.3}O_2$ Al-Doped	Pristine	2.8676	14.2298	101.4	2.35
	Charged 4.3 V after 5 cycles	2.8170	14.3431	98.6	1.78
	Discharged 3.0 V after 5 cycles	2.8676	14.2198	101.27	2.87

Thus, the modified interface comprising the Li$^+$-ion conducting active centers like LiAlO$_2$, AlF$_3$, Li[AlF$_4$], and AlPO$_4$ may promote enhanced Li$^+$ transport to the electrode bulk and to facilitate the charge-transfer reactions.[56] It should be emphasized that the above species can suppress, to some extent, the undesired side reactions at high anodic potentials, avoid the formation of resistive surface layers and therefore stabilize the electrode/solution interface. In general, they act as domains for the surface protection of the positive electrodes for Li-cells, the phenomenon that is well studied in the literature.[22–27] Note that our suggestions of the Al^{3+} enriched surface layer on the doped $LiNi_{0.5}Co_{0.2}Mn_{0.3}O_2$ particles are in line with the recently observed segregation of the dopant-ions like Cr^{3+}, Fe^{3+}, Ga^{3+} to the surface of spinel materials and of B or P-dopants near the surface of the crystalline silicon due to a strong thermodynamic driving force studied by time-of-flight secondary-ion mass spectrometry and first principles DFT calculations.[57,58] A similar phenomenon of the dopant cations (Ca, Sr, Ba) segregation resulting in more stable surfaces of cathodes for solid oxide fuel cells has been studied on the perovskite oxide.[59] These authors described the cation segregation in terms of the elastic and electrostatic interactions of the dopant with the surrounding lattice, which are the main driving forces for segregation. Since the dopant segregation is proposed to be chemically and structurally inhomogeneous in the form of surface clusters (domains) of the nm-size in height, their chemistry can be investigated by surface sensitive techniques, like XPS. In order to study the surface chemistry developed due to the interfacial reactions 2–6 and 10, we probed by XPS the Al-doped $LiNi_{0.5}Co_{0.2}Mn_{0.3}O_2$ particles after being in contact (aging) with EC-EMC/LiPF$_6$ solutions during 14 days (magnetic stirring, Argon atmosphere). The ratio of the $LiNi_{0.5}Co_{0.2}Mn_{0.3}O_2$ material to the solution volume was ∼15 mg/mL, similar to that in an electrochemical coin-type cell. The time of aging was equivalent to galvanostatic testing of the electrochemical cells containing $LiNi_{0.5}Co_{0.2}Mn_{0.3}O_2$ electrodes at a C/5 rate for ∼20 cycles. The results of XPS measurements of pristine and aged $LiNi_{0.5}Co_{0.2}Mn_{0.3}O_2$ materials are summarized in the Table II that includes binding energies and peak account of the relevant elements (XPS spectra are not shown for conciseness). From the comparative analysis of the spectral data of pristine samples we assume that a broad shoulder at ∼73–74.5 eV observed in the Al 2p spectrum of the Al-doped $LiNi_{0.5}Co_{0.2}Mn_{0.3}O_2$ can be assigned to Al-oxygen containing surface species (Al$_2$O$_3$) formed under ambient conditions though the dopant content is very minor. Upon aging in EC-DMC/LiPF$_6$ solution this shoulder of the Al 2p spectrum extends to much broader range of binding energies from ∼73.0 eV to ∼76.0 eV that match closely those for LiAlO$_2$, Al$_2$O$_3$ species and for a mixed aluminum oxide-fluoride Al$_2$O$_2$F$_2$. This later species can be formed by interactions of HF with Al(OH)$_3$ (reaction 3) or with Al$_2$O$_3$ like in the case of the Al$_2$O$_3$-coated LiMn$_{1.5}$Ni$_{0.5}$O$_4$ cycled cathode.[60] A weak peak at ∼77.4 eV in the Al 2p spectrum of the aged Al-doped $LiNi_{0.5}Co_{0.2}Mn_{0.3}O_2$ sample may relate to AlF$_3$. The fluorine spectrum F 1s measured from this sample confirms the formation of both AlF$_3$ (∼687.8 eV) and LiF (∼685.7 eV) surface species on the aged Al-doped $LiNi_{0.5}Co_{0.2}Mn_{0.3}O_2$ particles. The XPS spectra of oxygen O 1s of pristine samples demonstrate strong peaks at 531.7 eV that may reflect the surface oxygen, Li-carbonate, and LiOH. The formation of aluminum-fluorine containing species like AlF$_2$OH on the Al-doped aged particles is probably reflected by a shoulder at

533–533.5 eV of the O 1s spectrum. The XPS spectrum of Li 1s registered from the aged Al-doped sample also demonstrates the formation of surface LiF (peak at ∼56.7 eV), which partially substitutes Li$_2$O species (peak at ∼55 eV) developed possibly on the pristine particles during their synthesis. It is interesting to note that analysis of the phosphorus P 2p peaks of both undoped and Al-doped samples suggests surface species containing pentavalent phosphorous P^{5+}. In the case of undoped $LiNi_{0.5}Co_{0.2}Mn_{0.3}O_2$ particles the P 2p peak at 136 eV matches the binding energy for P–F bond (probably from PF$_6$ or PF$_5$ species) (also confirmed by ^{19}F SS NMR, as discussed below), while the phosphorus peak for the Al-doped aged material is shifted to 134 eV and may relate to species containing P–O–F bonds and to AlPO$_4$ formed according to the reaction 10.[61] The major broad peak at 854–857 eV in the spectrum of Ni 2p$_{3/2}$ measured from pristine Al-doped sample corresponds to the trivalent nickel in LiNiO$_2$.[62] For the aged sample, the shift to higher binding energy of ∼858 eV can be attributed to the partial nickel oxidation such as in LiNi$_x$Al$_y$O$_z$ species formed along with NiF$_2$ (857.4–858.2 eV).[63] Evidence for these species (LiNi$_x$Al$_y$O$_z$) is also confirmed via ^{7}Li solid state NMR, as discussed in the following section. Our XPS data show also that the oxidation state of the Mn is 4+ corresponding to the binding energy of 642.5–643 eV (Mn 2p$_{3/2}$) in the pristine sample, and this tetravalent state, as expected, is retained after aging the Al-doped $LiNi_{0.5}Co_{0.2}Mn_{0.3}O_2$ particles in solution. A peak at 655 eV of Mn 2p$_{1/2}$ in these spectra can also be ascribed to Mn^{4+}.[64] Note that a question may arise if the HF content in a real electrochemical cell would be sufficient to react with the "segregated" Al^{3+} ions of the doped $LiNi_{0.5}Co_{0.2}Mn_{0.3}O_2$ material to develop the surface species in reactions 2, 4, and 7, 10 detected by the XPS analysis? Simple calculations show that the hydrofluoric acid content is as large as 2.5·10^{-6} mol in 1 mL of an EC-EMC/LiPF$_6$ solution comprising ∼50 ppm of an unavoidably present HF. Then, note that 5–10 mg of the electrode active mass contains ∼0.5·10^{-6} – 1·10^{-6} mol Al^{3+}. This provides the HF:Al ratio ∼(5–2.5) : 1, making therefore the above surface reactions quite realistic due to the excess of HF. One should take into account also that the amount of HF in solution actually increases upon cycling, for instance by reaction 9.

Along with the different interfacial behavior of undoped and Al-doped $LiNi_{0.5}Co_{0.2}Mn_{0.3}O_2$ with solution species upon aging, these aged materials exhibited different thermal responses, as shown in Figure 9. The DSC curve *(a)* reflects the thermal decomposition of the EC-EMC/LiPF$_6$ solution alone that initiates at 185°C and exhibits an exothermic peak at 220°C. The total amount of the heat generated was 140 J g^{-1}. This exotherm is attributed to the redox reactions of LiPF$_6$ and its decomposition products, such as PF$_5$, with the alkyl carbonate solvents. The thermal behaviors of aged $LiNi_{0.5}Co_{0.2}Mn_{0.3}O_2$ undoped and Al-doped in contact with the electrolyte solution are presented in Figure 9 by DSC curves *(b)* and *(c),* respectively. In the I-st temperature range from 50 to 130°C, both aged undoped and Al-doped particles demonstrate *endothermic* peaks at ∼120°C (marked with red arrows) in reactions with the solution. The endothermic processes can be assigned to the dehydration of MnPO$_4$ · H$_2$O or MnHPO$_4$ · 3H$_2$O (detected by XRD and Raman spectroscopy on cycled/aged samples) and AlPO$_4$ · H$_2$O species formed,[65,66] for instance as a result of the reaction 10. We have shown previously that during aging of cathode materials Li[Ni-Co-Mn]O$_2$ in electrolyte solutions the reactions

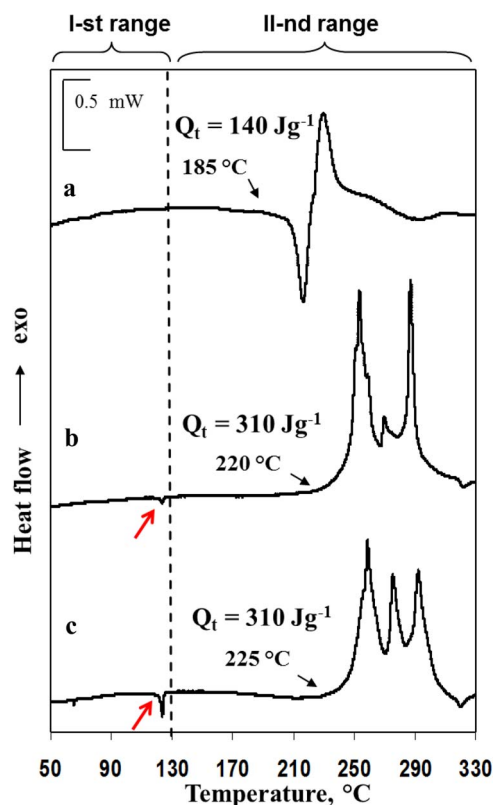**Figure 9.** Typical DSC responses measured upon heating of an EC:EMC/1M LiPF$_6$ solution alone *(a)* and of LiNi$_{0.5}$Co$_{0.2}$Mn$_{0.3}$O$_2$ undoped *(b)* and Al-doped *(c)* materials in the above solution. Prior to DSC measurements, these materials had been aged in EC:EMC/1M LiPF$_6$ solution in polyethylene vials at 30°C for 14 days (under magnetic stirring, in Ar atmosphere). The red arrows point to the endothermic reactions of the aged materials and solutions.

products are transition metal phosphate hydrates, as well as partially chemically delithiated phases and partially decomposed solutions.[67] The onset temperature of Mn and Al-hydrates dehydration in curves *(b)* and *(c)* is around 115°C, but the calculated heat is ~4 times higher in the case of the Al-doped aged material. This result can be explained by the additional contribution from the AlPO$_4$ · H$_2$O decomposition to the total heat of the endothermic reaction. It is important to note that other species, for instance AlF$_3$ formed upon the reaction 2, did not show any endothermic processes upon heating with the solution. This was demonstrated by measuring the DSC response from the artificially prepared mixture of undoped LiNi$_{0.5}$Co$_{0.2}$Mn$_{0.3}$O$_2$ containing AlF$_3$ (5 wt%). Further analysis of the thermal behavior of aged LiNi$_{0.5}$Co$_{0.2}$Mn$_{0.3}$O$_2$ materials in Figure 9 demonstrates that the endothermic reaction terminates and the system reaches an equilibrium state around 130°C. It remains stable up to the beginning of the solution decomposition at ~180°C. In the II-nd temperature range (130–330°C) both undoped and Al-doped aged materials (curves *(b)* and *(c)*), respectively, demonstrate three exothermic processes at ~260, 280, and 300°C. The calculated total heat is about 310 J/g in the both cases; however the structural transformations upon heating of these materials in solutions are different, as can be suggested from different rates of the exothermic reactions and from the redistribution of the total heat among three possible new phases formed. We propose that the increased amount of metal hydrates on the aged Al-doped LiNi$_{0.5}$Co$_{0.2}$Mn$_{0.3}$O$_2$ affects strongly the thermal processes in the high temperature range due to extensive endothermic decomposition reactions at low temperatures.

Solid state NMR studies of LiNi$_{0.5}$Co$_{0.2}$Mn$_{0.3}$O$_2$ samples.— As stated in the previous section, the NMR results are in good agreement with the other analytical data from this work. The ^{7}Li NMR single pulse spectra of the four samples are shown in Figure 10. The
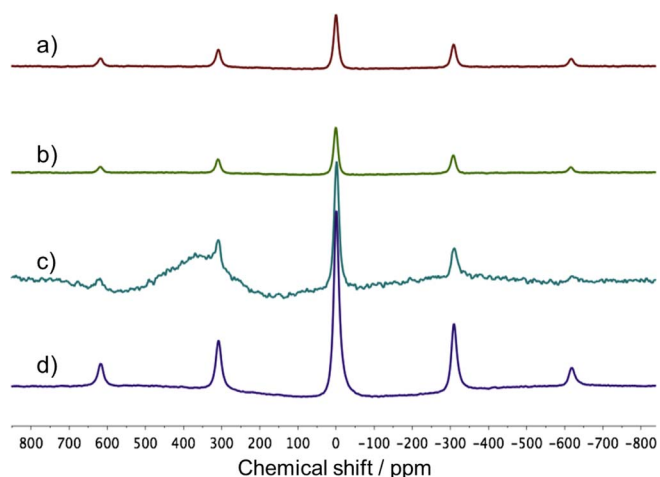

Figure 10. ^{7}Li MAS NMR single pulse data collected at 24 kHz spinning speed (normalized to rotor mass) from LiNi$_{0.5}$Co$_{0.2}$Mn$_{0.3}$O$_2$ materials: (a) Undoped, pristine, (b) Al-doped, pristine, (c) Undoped, cycled 100 times at a C/5 rate at 30°C and polarized to 3.0 V, (d) Al-doped, cycled 100 times at a C/5 rate at 30°C and polarized to 3.0 V.

spectra were collected under equivalent experimental conditions and normalized to the mass in the rotor. All four spectra indicate a narrow resonance with similar spinning sideband manifolds centered at 0 ppm, representing lithium in a diamagnetic environment. In the pristine materials, this resonance is attributed to Li found in a diamagnetic environment, such as LiOH, that may be formed as by-product of the materials' synthesis, and possibly also represents Li atoms in segregated regions of (diamagnetic) LiCoO$_2$. In the cycled materials, this same signal is attributed to lithium in similar environments to those observed in the pristine case, in addition to the Li-species in the SEI on the electrode's surface (e.g. Li$_2$O, LiF, and other species already identified and reported before.[48,68,69] The remaining, structural, lithium is typically NMR-invisible in single-pulse experiments such as these. This is because of the strong effect of paramagnetic Ni^{2+} and Mn^{4+} ions surrounding these lithium ions inducing rapid dephasing of the ^{7}Li magnetization, thereby diminishing most, if not all, of the signal within the unavoidable post-pulse dead-time of the probe (6.5 μs). Such resonances are usually in the 300 to 2000+ ppm range.[70] However, in this set of data, a paramagnetically shifted resonance was observed - a broad line centered on 350 ppm - seen only in the undoped, cycled material. The implication of the visibility of this shift in the single-pulse experiment is that the lithium species associated with this peak experience a weaker paramagnetic effect, i.e. the immediate lithium environment of this material does *not* contain any of the highly paramagnetic Mn^{4+} ions. The size of the shift is suggestive of small domains of LiNiO$_2$ and/or LiCoNiO$_2$ species, relatively isolated from the bulk species (more specifically, the Mn^{4+}). It is most reasonable to presume that such domains are located on or close to the cathode surface, formed from nickel (and possibly cobalt) ions that leached out of the bulk. Previous studies on LiNi$_{0.8}$Co$_{0.2}$O$_2$ and LiNi$_{0.3}$Mn$_{0.3}$Co$_{0.3}$O$_2$ cathodes have shown a similar process of Ni leaching out of the bulk.[9,71] As is clear from the figure, this feature is only detected in the undoped material, suggesting that this phenomenon is markedly reduced by the presence of the Al dopant. This result is in agreement with the XPS data, as described above.

Generally, rotor-synchronized spin-echo sequences collected at very high spinning rates are used to overcome the limitation of the NMR-invisibility of fast-dephasing bulk lithium in paramagnetic environments.[72] The Hahn echo sequence serves to re-focus the inhomogeneous dephasing mechanisms, thereby recovering much of the otherwise-invisible signal. Such spectra were taken of these samples (data not shown) and revealed, as expected, a broad line centered around 350 ppm, with the spinning sidebands of the narrow diamagnetic resonance sitting on top, similarly to previously published data
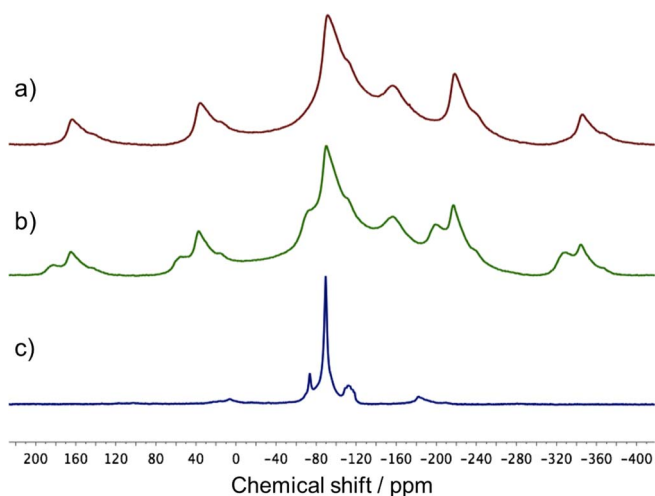
Figure 11. ^{19}F MAS NMR single pulse data collected at 24 kHz spinning speed, (normalized to rotor mass) from LiNi$_{0.5}$Co$_{0.2}$Mn$_{0.3}$O$_2$ materials: (a) Undoped, cycled 100 times at a C/5 rate at 30°C and polarized to 3.0 V, (b) Al-doped cycled 100 times at a C/5 rate at 30°C and polarized to 3.0 V, (c) measured from PVdF (Kynar 2801).

on (aged) Li(Ni$_{1-y-z}$Co$_y$Al$_z$)O$_2$ by Menetrier et al.[73] (It should be noted that the main peak observed in their study was seen near 400 ppm, owing to the bulk material being of slightly different composition). Here, it is observed as well that the paramagnetically shifted peak in the pristine material, representing the lithium in the bulk material, is both narrower and more intense in absolute terms, as compared to the cycled sample. This reflects the reduction in reversible capacity of the electrode, as it is a quantitative measure of the reduced re-lithiation of the active material. At the same time, the 0 ppm feature seen in both samples is stronger in the aluminum-doped material, indicating that more surface Li is found upon electrode cycling. This Hahnecho data is not shown, as it did not reveal any new information.

The ^{19}F single-pulse MAS NMR data is shown in Figure 11. Only the cycled samples were fluorine-containing (the only source of fluorine in these cells being the PVdF and the LiPF$_6$ salt). The signals near −105 and −165 ppm seen in both samples are background signals from the stator material. These background signals are quite intense and broad, therefore anything which is expected to resonate in that vicinity (LiAlF$_4$, at −155 ppm, AlF$_3$, at −173 ppm or LiF at −200 ppm) will not be discernible in small quantities (less than 5%). As expected, the strongest signal seen in both samples is the PVdF material, as it makes up 10% of the electrode sample weight. Because of this, it can also serve as an internal quantitative absolute reference. The PVdF used in the sample preparation was examined separately and in the pristine form indicates at least 3 resonances: the main peak at −99.2 ppm, assigned to the bulk head-tail (H-T) polymeric units (-CH$_2$-CF$_2$-), a smaller shoulder at −119 ppm, assigned to H-H/T-T subunits (-CF$_2$CF$_2$CH$_2$CH$_2$-) and another minor peak at −73 ppm, probably a PVdF defect site.[74] Of these, the former two resonances are clearly seen in both cycled samples. The most significant difference seen in the two cycled samples is the presence of the −73 ppm peak, which is seen only in the Al-doped sample. Given the high electrochemical, chemical, and thermal stability of PVdF, it is unlikely that this is an increase in the PVdF defect site (as it is assigned above in the PVdF spectra), and more likely attributed to PF$_5$, which also resonates at this chemical shift.[75] In the cycled undoped material, it is not present at higher than 6–7% of the main PVdF peak, and in the doped sample, it is measured as almost 40% the size of the main peak. It appears that the presence of aluminum has some effect on the breakdown pathway of the LiPF$_6$ salt, likely acting as a catalyst for its decomposition to PF$_5$, and/or preventing its further breakdown to PF$_3$ and POF$_3$ groups, as described in the suggested reactions listed above.

^{27}Al MAS NMR data was collected on the pristine, Al-doped sample, in which a single broad peak (half-height width 2 kHz) was seen in the solid echo experiment at −14 ppm. This data (not shown) is indicative of aluminum in a salt form, i.e. surface aluminum-containing species. Evidence for aluminum in the bulk was not seen in the NMR data that was collected. This may be a result of severe spectral broadening due to the quadrupolar interactions of the ^{27}Al nuclei in an asymmetrical environment, or simply insufficient signal due to extremely small quantities of aluminum in that configuration.

Structural characterization of LiNi$_{0.5}$Co$_{0.2}$Mn$_{0.3}$O$_2$ materials and electrodes at various states of charge (XRD, TEM-ED analyses).— A detailed structural characterization of the doped and undoped pristine materials was carried out by Rietveld method. The model used for the Rietveld refinement based on the layered rhombohedral NaFeO$_2$-type structure (*R-3m* space group), in which the octahedral *3b* iron sites were occupied by Ni^{2+}, Mn^{4+} and Co^{3+} ions, whereas Li$^+$ ions were positioned on the octahedral *3a* sodium sites thus forming lithium layers. The occupancy ratios for transition metals at *3b* site were constrained to the values corresponding to the chemical formula of the material. After preliminary refinement of the lattice parameters and obtaining the isotropic atomic displacement parameters the values of B_{iso} were fixed, and, assuming the presence of extra Ni^{2+} ions in the lithium layer, we varied the occupancy of Li$^+$/Ni^{2+} ions at *3a* lithium site. In the case of Al-doped material we also considered possible replacing Co^{3+} ions with Al^{3+} ions at *3b* site; it was found that the contribution of the substituent Al ions to the occupancy of transition metal layers is about 0.01%, which corresponds to Al content of about 0.0004 Al ions/unit cell. The refined occupancies for Li$^+$/Ni^{2+} ions at *3a* site yielded the Ni-to-Li ratio about 0.01/98.8 both for doped and undoped materials. An agreement between the experimental and the calculated diffraction patterns was rather good (Figure 12a, 12b), with reliability factors R$_b$ = 8.5% and R$_b$ = 5.5%, respectively for doped and undoped cases. The results of Rietveld analysis indicated a pronounced layered character of the structure of the pristine materials (doped and undoped) with good separation of transition metal ions and Li ions onto their respective planes. Low values of the ratio of the integral intensities of [102], [006] and [101] peaks (I$_{102}$+I$_{006}$)/I$_{101}$, which were, respectively equal to 0.37 and 0.40 for Al-doped and undoped pristine materials, provided an additional indicative of the good quality of their layered structure. Changes in the XRD patterns produced by charge/discharge cycling of LiNi$_{0.5}$Co$_{0.2}$Mn$_{0.3}$O$_2$ electrodes with final charge to 4.3 V (red profiles) and by cycling ended by discharge to 3.0 V (green profiles) are presented in Figure 13a and 13b, relating to doped and undoped materials, respectively. It can be seen that the patterns obtained from the cycled samples contain all the diffraction peaks of pristine and do not show formation of any additional phase, thus implying that the original layered structure described by *R-3m* space group is retained. The only additional peak labeled G at 2θ = 26.5° arises from remnants of graphite in the electrode. We observe, however, a noticeable shift of the diffraction peaks, with respect to pristine, in the profiles (in red color) obtained from both doped and undoped materials, which were subjected to charge/discharge cycling terminated by charge to 4.3 V. In these profiles the distance between the pairs of peaks (018)/(110) and (006)/(012) increases, and, in fact, the peak (006) merges with reflection (101). This shift indicates changes in the lattice parameters, which were apparently caused by the delithiation process in the course of the final charge to 4.3 V. When electrochemical cycling is completed by subsequent discharge, lithium ions intercalate back to their octahedral sites in the layered structure (*R-3m*), and the unit cell of the material should be restored approximately to its initial dimensions, meaning the diffraction peaks will move back toward their former positions. This is exactly what we observe in the green profiles in Figure 13a and 13b: peak (006) appears again, and the (018)/(110) peaks become close to their positions in pristine material. Table II shows the results of least-square refinement of lattice parameters characterizing each XRD profile. It follows from Table II that the unit cell volume of both Al-doped and undoped materials decreases after cycling terminated by charge to 4.3 V, apparently due to extraction
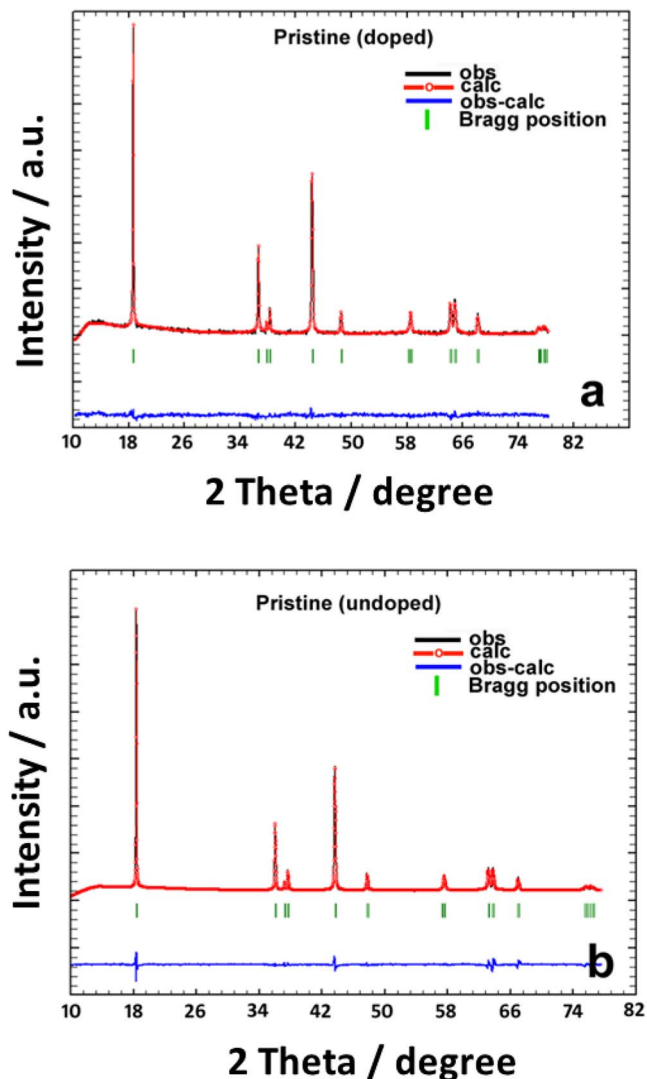
Figure 12. Rietveld refinement plots obtained for pristine $LiNi_{0.5}Co_{0.2}Mn_{0.3}O_2$: (a) Al-doped material; (b) undoped material.

Figure 13. Changes in the XRD patterns produced by charge/discharge cycling of (a) Al-doped and (b) undoped materials. Peak labeled as "G" is due to the graphite additive to the electrode mass.

of lithium during final charging. Correspondingly, the *a*-lattice parameter decreases because the distance between transition metal ions reduces as a result of their oxidation, albeit the *c*-lattice parameter increases. When the lithium ions intercalate to the structure during the final discharge, the unit cell volume is restored almost completely. Ac-
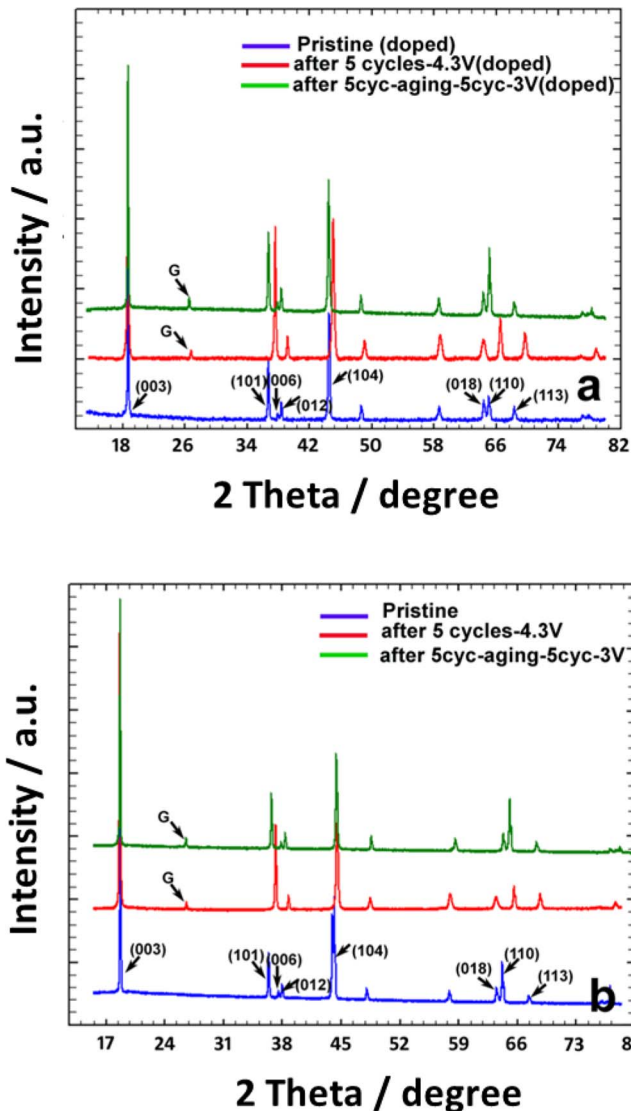
cordingly, the unit cell dimensions get closer to the cell parameters of pristine.

The results of TEM observations of samples are consistent with the structural information obtained by XRD. Using convergent-beam
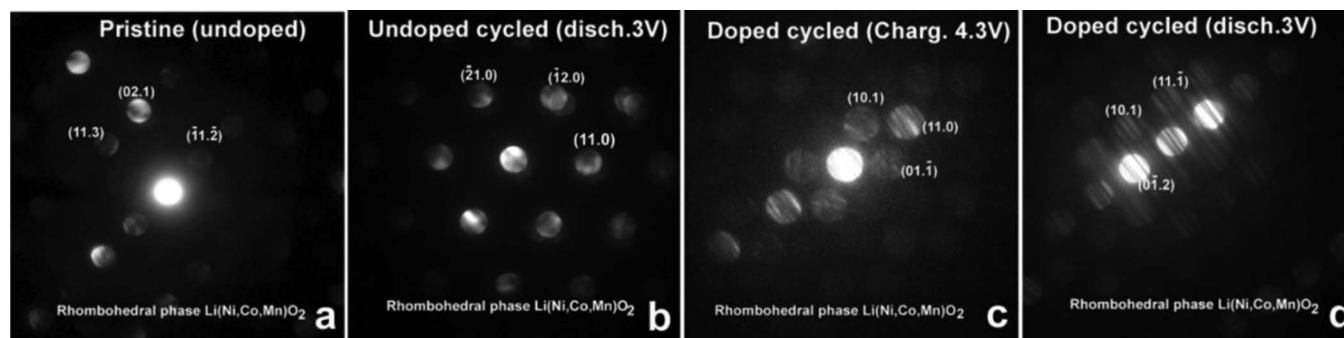

Figure 14. Examples of CBED patterns demonstrating that in the vast majority of the analyzed particles of both Al-doped and undoped materials the original layered structure (*R-3m*) is retained upon cycling. (a) CBED pattern from undoped pristine; (b) CBED pattern from undoped material after cycling terminated by discharge to 3.0 V; (c) CBED pattern from Al-doped material after cycling terminated by charge to 4.3 V; (d) CBED pattern from Al-doped material after cycling terminated by discharge to 3.0 V.
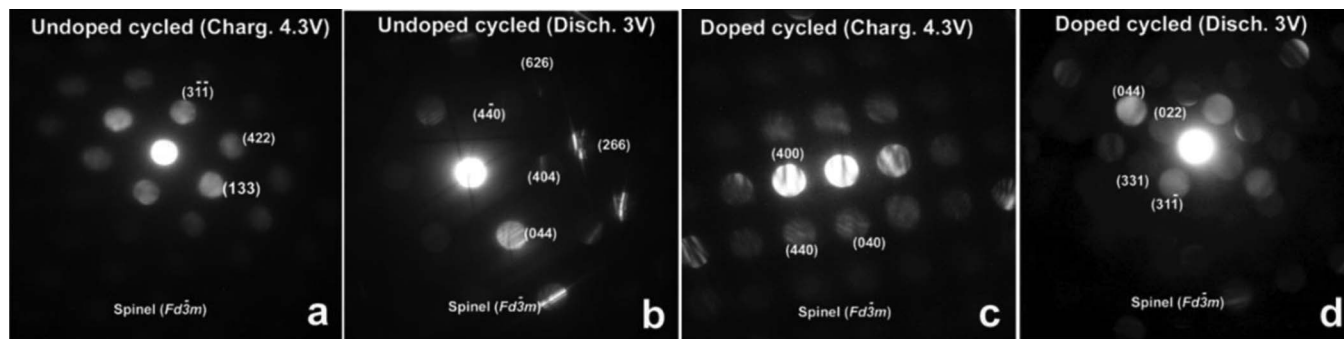
Figure 15. Examples of CBED diffractions demonstrating the existence of cubic spinel structure in the cycled material. (a) CBED pattern from the spinel particle formed in undoped material after cycling terminated by charge to 4.3 V; (b) CBED pattern from the spinel particle observed in undoped material subjected to cycling ended by discharge to 3.0 V; (c) CBED pattern from the spinel particle formed in Al-doped material after cycling terminated by charge to 4.3 V; (d) CBED pattern showing the presence of spinel particle in Al-doped material after cycling terminated by discharge to 3.0 V.

electron diffraction technique we analyzed several tens of individual particles representing doped and undoped materials in their initial state (pristine) and also after electrochemical cycling. Examples of CBED patterns taken from the particles of doped and udoped cycled materials are shown in Figure 14a–14d. All these patterns were indexed in terms of the rhombohedral structure Li(TM)O_2 thus demonstrating that the original layered structure of pristine described by *R-3m* space group is retained upon cycling. Though examination of the XRD patterns taken from cycled samples has shown that they can be considered as single phase material possessing the layered α-NaFeO_2–type (*R-3m*) struc-

Figure 16. Typical DSC responses measured upon heating in EC:EMC/1M LiPF$_6$ solution of LiNi$_{0.5}$Co$_{0.2}$Mn$_{0.3}$O$_2$ electrodes comprising undoped and Al-doped materials: (a) undoped pristine electrode, (b) undoped electrode cycled at 30°C and charged to 4.3 V after the 5-th cycle, (c) Al-doped pristine electrode, (d) Al-doped electrode cycled at 30°C and charged to 4.3 V after the 5-th cycle.

ture, some CBED patterns straightforwardly revealed the presence of trace amounts of cubic spinel structure. Shown in Figure 15a–15d CBED diffractions demonstrate unequivocally the existence of cubic spinel phase as a result of layered-to-spinel structural transformation in the cycled material. It is worth noting that the EDS analysis of the particles that were identified as possessing spinel structure shows that their composition noticeably differs from the composition of the pristine material by the Ni/Ni+Co+Mn ratio. This may relate to different energetic activation barriers for Ni, Co, and Mn to migrate to the lithium sites upon Li$^+$ deintercalation.[76,77]
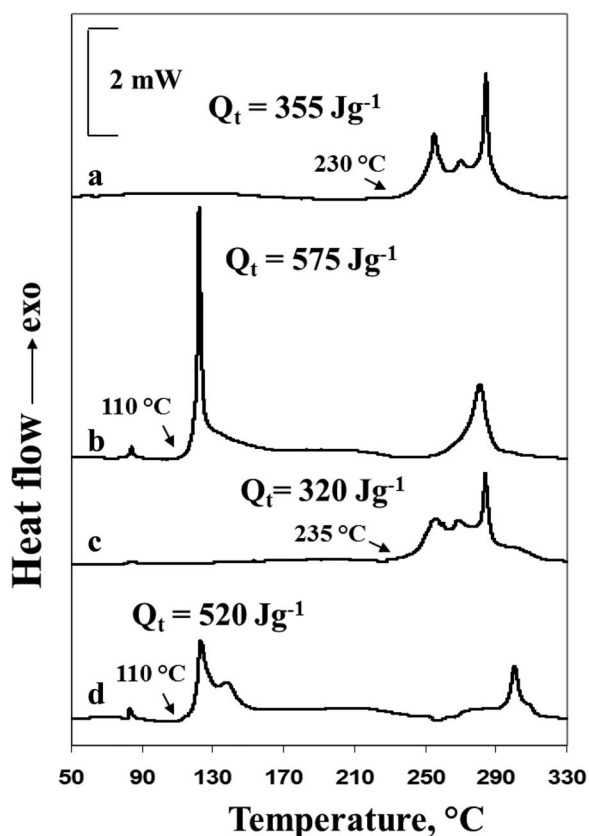
Thermal behavior of LiNi$_{0.5}$Co$_{0.2}$Mn$_{0.3}$O$_2$ electrodes.— DSC profiles of pristine LiNi$_{0.5}$Co$_{0.2}$Mn$_{0.3}$O$_2$ materials Al-doped and undoped in contact with 1M LiPF$_6$/EC: EMC 3:7 solution are shown in Figure 16. The DSC response of the pristine undoped material upon heating in the above solution demonstrates at least three reactions started at 230°C and accompanied with heat evolution about 355 J/g (Figure 16, curve *a*). The exothermic reactions between the electrolyte and the cathode materials at elevated temperatures occur due to oxidization of the solvents by oxygen released from the electrode material. The delithiated undoped material (curve *b*) shows the first exothermic reaction around 75°C related to decomposition of the electrode passive layer formed upon cycling. The characteristics of the main exothermic processes of this material are a decrease of the onset temperature to ∼110°C and the overall heat of 575 J/g, much higher than of the pristine material. A comparison of the DSC thermogramms *(a)* and *(c)* demonstrates that the thermal behavior of the Al-doped pristine LiNi$_{0.5}$Co$_{0.2}$Mn$_{0.3}$O$_2$ electrode is characterized by a slight increase of the onset temperature but a decrease of the total heat (320 J/g). It was established that the DSC response of the delithiated Al-doped material (curve *d*) is similar to that of the undoped one, however the total exothermic heat evolved decreased to ∼520 J/g indicating thus more stable thermal behavior of the doped sample in a charged state. We note that both undoped and doped materials demonstrate the same number of the exothermic peaks during heating with electrolyte solution. These peaks are attributed to structural transformations of the materials upon heating. However, the shape of the exothermic peaks of the Al-doped material measured both in pristine and in charged state (4.3 V) are broader as compared to the undoped. This may indicate lower rates of the thermal reactions between the Al-doped LiNi$_{0.5}$Co$_{0.2}$Mn$_{0.3}$O$_2$ and solution species and therefore higher thermal stability of this material.

Conclusions

In this work, we studied the electrochemical behavior, as well as the structural and thermal characteristics of the Ni-rich LiNi$_{0.5}$Co$_{0.2}$Mn$_{0.3}$O$_2$ undoped and Al-doped materials for positive electrodes of lithium batteries. It was established based on the results of Rietveld profile fitting that the structural features of these materials

are quite identical from the crystallographic point of view. Indeed, the pure $LiNi_{0.5}Co_{0.2}Mn_{0.3}O_2$ and the Al-doped materials differ only by a minute amount of dopant ($\sim$0.01 at.%). These materials are of layered rhombohedral α-$NaFeO_2$-type structure (*R-3m* space group) and possess similar lattice parameters and equal "slab thickness Li/TM" and "Li/TM" ratios, as well as the g-factor around 2.05 measured by EPR for both undoped and Al-doped $LiNi_{0.5}Co_{0.2}Mn_{0.3}O_2$. Using DFT, we calculated the most preferred Al-doped configurations. The lowest energy was found for the Ni substituted configuration, in which Al^{+3} is surrounded by 1 Co, 2 Mn and 3 Ni ions. It was also demonstrated that Al substitution in the doped $LiNi_{0.5}Co_{0.2}Mn_{0.3}O_2$ is preferred at Ni sites over Co sites, and the thermodynamic preference for Al^{3+} substitutions follows the order: Ni>Co>Mn. From the electrochemical studies of undoped and Al-doped $LiNi_{0.5}Co_{0.2}Mn_{0.3}O_2$ electrodes at 30, 45, and 60°C we conclude that these electrodes exhibit similar irreversible capacity loss (ICL) during the first charge/discharge. It is suggested that the decreasing ICL for both types of electrodes, as the temperature increases, may be related to reduced side-reactions. We propose that the reduced side-reactions are a result of effective passivation of the electrode surface at higher temperatures due to the optimized properties of the surface films naturally formed on these cathode materials in standard electrolyte solutions. We propose that the lower capacity fading of the Al-doped electrodes upon aging of the cells in a charged state (4.3 V) at 60°C in comparison with their undoped counterparts, as well as more stable mean voltage behavior, are likely due to the chemical and structural modifications of the electrode/solution interface upon cycling and storage of the Al-doped electrodes. An interesting finding from this work is that upon short-term cycling tests, the Al-doped $LiNi_{0.5}Co_{0.2}Mn_{0.3}O_2$ electrodes demonstrate lower activation energies for the discharge process. This correlates well with the results of our solid state NMR studies of the ^7Li spectra for undoped and Al-doped materials subjected to electrochemical cycling. We have found that the broad NMR line with a peak at $\sim$350 ppm (paramagnetically shifted) appeared in the Li spectrum of the undoped cycled material. The lithium ions associated with this peak experience a weaker paramagnetic effect than would be experienced if Mn^{4+} ions are found in their closest shell. Weak interactions with Ni^{2+} ions may be from Li-[Ni-(Co)-]O_2 species located on the cathode surface formed as a consequence of nickel (and possibly cobalt) leach out from the bulk, in agreement with the literature data. Our suggestion is that the leached ions form Ni-rich domains on the cycled undoped material surface, which partially interfere with the Li^+ diffusion in and out of the $LiNi_{0.5}Co_{0.2}Mn_{0.3}O_2$ electrodes. The Al^{3+} doping inhibits Ni leaching, thus promoting faster Li-transport and lower activation energy of discharge in the case of doped $LiNi_{0.5}Co_{0.2}Mn_{0.3}O_2$. We also conclude that the electrochemical behavior of Al-doped $LiNi_{0.5}Co_{0.2}Mn_{0.3}O_2$ electrodes correlates with the lower resistances of the Li^+ migration through the surface films and of the charge-transfer measured at 3.9 V and 4.3 V after cycling and aging in a charged state. The lower impedances of Al-doped $LiNi_{0.5}Co_{0.2}Mn_{0.3}O_2$ electrodes can be explained by more stable surface chemistry developed on the doped particles due to the interfacial reactions of the dopant in Al^{3+} enriched surface layer ("segregated" aluminum) with an EC-EMC/$LiPF_6$ solution. It is concluded from electrochemical impedance and XPS studies that the modified stable and less resistive interface on the Al-doped particles comprises the Li^+-ion conducting nano-sized centers like $LiAlO_2$, AlF_3, etc., which promote Li^+ ionic transport to the bulk and therefore facilitate the electrochemical reactions. A correlation was also established between the modified interface of the Al-doped $LiNi_{0.5}Co_{0.2}Mn_{0.3}O_2$ particles aged in an EC-EMC/$LiPF_6$ solution and their thermal responses. We suggest from DSC experiments that much higher the endothermic heat reverted at $\sim$120°C of the doped particles, aged in solutions, comparing to the undoped ones, relates to the dehydration reactions of the surface accumulated Mn- and Al-phosphates formed upon aging. It was found from X-ray and electron diffraction studies that the cycled $LiNi_{0.5}Co_{0.2}Mn_{0.3}O_2$ samples retain mainly their original layered structure described by the *R-3m* space group. At the same time, we established unambiguously the formation of

a cubic spinel structure (*Fd-3m*) in cycled electrodes (both undoped and Al-doped samples) due to the layered-to-spinel transition upon Li-extraction. The elemental compositions of these spinel structures were found to be significantly different to those of the pristine layered Li[NiCoMn]O_2 material. This effect deserves a separate examination and will be studied further by our groups.

References

1. J. M. Tarascon and M. Armand, *Nature*, **414**, 359 (2001).
2. M. S. Whittingham, *Chem. Rev.*, **104**, 4271 (2004).
3. J. B. Goodenough and Y. Kim, *Chem. Mater.*, **22**, 587 (2009).
4. A. Manthiram, *J. Phys. Chem. Lett.*, **2**, 176 (2011).
5. M. M. Thackeray, C. Wolverton, and E. D. Isaacs, *Energy Environ. Sci.*, **5**, 7854 (2012).
6. E. M. Erickson, C. Ghanty, and D. Aurbach, *J. Phys. Chem. Lett.*, **5**, 3313 (2014).
7. V. Etacheri, R. Marom, R. Elazari, G. Salitra, and D. Aurbach, *Energy Environ. Sci.*, **4**, 3243 (2011).
8. C. H. Chen, J. Liu, M. E. Stoll, G. Henriksen, D. R. Vissers, and K. Amine, *J. Power Sources*, **128**, 278 (2004).
9. H. Liu, Z. Zhang, Z. Gong, and Y. Yang, *Solid State Ionics*, **166**, 317 (2004).
10. J. W. Fergus, *J. Power Sources*, **195**, 939 (2010).
11. T. Akita, M. Tabuchi, Y. Nabeshima, K. Tatsumi, and M. Kohyama, *J. Power Sources*, **254**, 39 (2014).
12. W. El Mofid, S. Ivanov, A. Konkin, and A. Bund, *J. Power Sources*, **268**, 414 (2014).
13. W. Zhu, D. Liu, J. Trottier, C. Gagnon, A. Guerfi, C. M. Julien, A. Mauger, and K. Zaghib, *J. Power Sources*, **264**, 290 (2014).
14. S. H. Kang and K. Amine, *J. Power Sources*, **119–121**, 150 (2003).
15. S.-T. Myung, S. Komaba, N. Hirosaki, K. Hosoya, and N. Kumagai, *J. Power Sources*, **146**, 645 (2005).
16. Y. Zhang and C.-Y. Wang, *J. Electrochem. Soc.*, **156**, A527 (2009).
17. M. Mladenov, R. Stoyanova, E. Zhecheva, and S. Vassilev, *Electrochem. Commun.*, **3**, 410 (2001).
18. E.-S. Lee and A. Manthiram, *J. Mater. Chem. A*, **1**, 3118 (2013).
19. Y.-D. Cho, G.-K. Fey, and H.-M. Kao, *J. Solid State Electrochem.*, **12**, 815 (2008).
20. Y.-S. He, L. Pei, X.-Z. Liao, and Z.-F. Ma, *J. Fluor. Chem.*, **128**, 139 (2007).
21. L. Croguennec, J. Bains, M. Ménétrier, A. Flambard, E. Bekaert, C. Jordy, P. Biensan, and C. Delmas, *J. Electrochem. Soc.*, **156**, A349 (2009).
22. S.-T. Myung, K. Izumi, S. Komaba, Y.-K. Sun, H. Yashiro, and N. Kumagai, *Chem. Mater.*, **17**, 3695 (2005).
23. K. Amine, H. Yasuda, and M. Yamachi, *Electrochem. Solid State Lett.*, **3**, 178 (2000).
24. M. M. Thackeray, C. S. Johnson, J. S. Kim, K. C. Lauzze, J. T. Vaughey, N. Dietz, D. Abraham, S. A. Hackney, W. Zeltner, and M. A. Anderson, *Electrochem. Commun.*, **5**, 752 (2003).
25. J. Liu and A. Manthiram, *J. Mater. Chem.*, **20**, 3961 (2010).
26. S. K. Martha, J. Nanda, Y. Kim, R. R. Unocic, S. Pannala, and N. J. Dudney, *J. Mater. Chem. A*, **1**, 5587 (2013).
27. Y.-K. Sun, M.-J. Lee, C. S. Yoon, J. Hassoun, K. Amine, and B. Scrosati, *Adv. Mater.*, **24**, 1192 (2012).
28. N.-S. Choi, Z. Chen, S. A. Freunberger, X. Ji, Y.-K. Sun, K. Amine, G. Yushin, L. F. Nazar, J. Cho, and P. G. Bruce, *Angew. Chem. Int. Ed.*, **51**, 9994 (2012).
29. N. Kosova, E. Devyatkina, A. Slobodyuk, and V. Kaichev, *Solid State Ionics*, **179**, 1745 (2008).
30. J. Cho, T.-J. Kim, Y. J. Kim, and B. Park, *Electrochem. Solid State Lett.*, **4**, A159 (2001).
31. F. Amalraj, M. Talianker, B. Markovsky, L. Burlaka, N. Leifer, G. Goobes, E. M. Erickson, O. Haik, J. Grinblat, E. Zinigrad, D. Aurbach, J. K. Lampert, J.-Y. Shin, M. Schulz-Dobrick, and A. Garsuch, *J. Electrochem. Soc.*, **160**, A2220 (2013).
32. W. Kraus and G. Nolze, *J. Appl. Crystallogr.*, **29**, 301 (1996).
33. J. Rodríguez-Carvajal, *Physica B*, **192**, 55 (1993).
34. H. Gabrisch, T. Yi, and R. Yazami, *Electrochem. Solid State Lett.*, **11**, A119 (2008).
35. G. Kresse and J. Hafner, *Phys. Rev. B*, **47**, 558 (1993).
36. G. Kresse and J. Hafner, *Phys. Rev. B*, **49**, 14251 (1994).
37. J. P. Perdew, J. A. Chevary, S. H. Vosko, K. A. Jackson, M. R. Pederson, D. J. Singh, and C. Fiolhais, *Phys. Rev. B*, **48**, 4978 (1993).
38. P. E. Blöchl, *Phys. Rev. B*, **50**, 17953 (1994).
39. W.-S. Yoon, S. Iannopollo, C. P. Grey, D. Carlier, J. Gorman, J. Reed, and G. Ceder, *Electrochem. Solid State Lett.*, **7**, A167 (2004).
40. Y. S. Meng, G. Ceder, C. P. Grey, W.-S. Yoon, and Y. Shao-Horn, *Electrochem. Solid State Lett.*, **7**, A155 (2004).
41. F. Weill, N. Tran, L. Croguennec, and C. Delmas, *J. Power Sources*, **172**, 893 (2007).
42. P. S. Whitfield, I. J. Davidson, L. M. D. Cranswick, I. P. Swainson, and P. W. Stephens, *Solid State Ionics*, **176**, 463 (2005).

43. D. Zeng, J. Cabana, J. Bréger, W.-S. Yoon, and C. P. Grey, *Chem. Mater.*, **19**, 6277 (2007).
44. H. Yu, Y. Qian, M. Otani, D. Tang, S. Guo, Y. Zhu, and H. Zhou, *Energy Environ. Sci.*, **7**, 1068 (2014).
45. B. J. Hwang, Y. W. Tsai, D. Carlier, and G. Ceder, *Chem. Mater.*, **15**, 3676 (2003).
46. Y. Koyama, N. Yabuuchi, I. Tanaka, H. Adachi, and T. Ohzuku, *J. Electrochem. Soc.*, **151**, A1545 (2004).
47. Y. Makimura and T. Ohzuku, *J. Power Sources*, **119–121**, 156 (2003).
48. D. Aurbach, *J. Power Sources*, **89**, 206 (2000).
49. B. Zhang, G. Chen, P. Xu, and C. C. Li, *J. Power Sources*, **176**, 325 (2008).
50. A. J. Bard and L. R. Faulkner, *Electrochemical Methods: Fundamentals and Applications*, Wiley (2000).
51. S.-T. Myung, N. Kumagai, S. Komaba, and H.-T. Chung, *Solid State Ionics*, **139**, 47 (2001).
52. D. Li, Y. Sasaki, K. Kobayakawa, and Y. Sato, *J. Power Sources*, **157**, 488 (2006).
53. B. Zhang, G. Chen, Y. Liang, and P. Xu, *Solid State Ionics*, **180**, 398 (2009).
54. X. Liu, T. Huang, and A. Yu, *Electrochim. Acta*, **133**, 555 (2014).
55. R. E. Kirk, D. F. Othmer, J. I. Kroschwitz, and M. Howe-Grant, *Encyclopedia of chemical technology*, Wiley (1998).
56. B. C. Park, H. B. Kim, S. T. Myung, K. Amine, I. Belharouak, S. M. Lee, and Y. K. Sun, *J. Power Sources*, **178**, 826 (2008).
57. D. W. Shin, C. A. Bridges, A. Huq, M. P. Paranthaman, and A. Manthiram, *Chem. Mater.*, **24**, 3720 (2012).
58. B. R. Long, M. K. Y. Chan, J. P. Greeley, and A. A. Gewirth, *J. Phys. Chem. C*, **115**, 18916 (2011).
59. W. Lee, J. W. Han, Y. Chen, Z. Cai, and B. Yildiz, *J. Am. Chem. Soc.*, **135**, 7909 (2013).
60. L. Baggetto, N. J. Dudney, and G. M. Veith, *Electrochim. Acta*, **90**, 135 (2013).
61. T. Lindblad, B. Rebenstorf, Z.-G. Yan, and S. L. T. Andersson, *Appl. Catal. A,* **112**, 187 (1994).
62. A. N. Mansour, *Surf. Sci. Spectra*, **3**, 279 (1994).
63. A. P. Grosvenor, M. C. Biesinger, R. S. C. Smart, and N. S. McIntyre, *Surf. Sci.*, **600**, 1771 (2006).
64. B. J. Tan, K. J. Klabunde, and P. M. A. Sherwood, *J. Am. Chem. Soc.*, **113**, 855 (1991).
65. L. Wang, W. Sun, J. Li, J. Gao, X. He, and C. Jiang, *Int. J. Electrochem. Sci*, **7**, 3591 (2012).
66. K. Tsutsumi, K. Mizoe, and K. Chubachi, *Colloid Polym. Sci.*, **277**, 83 (1999).
67. S. K. Martha, B. Markovsky, J. Grinblat, Y. Gofer, O. Haik, E. Zinigrad, D. Aurbach, T. Drezen, D. Wang, G. Deghenghi, and I. Exnar, *J. Electrochem. Soc.*, **156**, A541 (2009).
68. M. Balasubramanian, H. S. Lee, X. Sun, X. Q. Yang, A. R. Moodenbaugh, J. McBreen, D. A. Fischer, and Z. Fu, *Electrochem. Solid State Lett.*, **5**, A22 (2002).
69. A. M. Andersson, D. P. Abraham, R. Haasch, S. MacLaren, J. Liu, and K. Amine, *J. Electrochem. Soc.*, **149**, A1358 (2002).
70. C. P. Grey and Y. J. Lee, *Solid State Sci.*, **5**, 883 (2003).
71. O. Haik, N. Leifer, Z. Samuk-Fromovich, E. Zinigrad, B. Markovsky, L. Larush, Y. Goffer, G. Goobes, and D. Aurbach, *J. Electrochem. Soc.*, **157**, A1099 (2010).
72. W.-S. Yoon, C. P. Grey, M. Balasubramanian, X.-Q. Yang, D. A. Fischer, and J. McBreen, *Electrochem. Solid-State Lett.*, **7**, A53 (2004).
73. M. Ménétrier, C. Vaysse, L. Croguennec, C. Delmas, C. Jordy, F. Bonhomme, and P. Biensan, *Electrochem. Solid-State Lett.*, **7**, A140 (2004).
74. T.-W. Su and D.-L. M. Tzou, *Polymer*, **41**, 7289 (2000).
75. U. S. B. Department of Chemistry and Biochemistry, 19F Chemical Shifts and Coupling Constants.
76. A. Van der Ven and G. Ceder, *Electrochem. Solid-State Lett.*, **3**, 301 (2000).
77. S. P. Ong, V. L. Chevrier, G. Hautier, A. Jain, C. Moore, S. Kim, X. Ma, and G. Ceder, *Energy Environ. Sci.*, **4**, 3680 (2011).